

REPORT DOCUMENTATION PAGE

AFRL-SR-AR-TR-04-

The public reporting burden for this collection of information is estimated to average 1 hour per response, including the gathering and maintaining the data needed, and completing and reviewing the collection of information. Send comments or information, including suggestions for reducing the burden, to Department of Defense, Washington Headquarters (0704-0188), 1215 Jefferson Davis Highway, Suite 1204, Arlington, VA 22202-4302. Respondents should be aware subject to any penalty for failing to comply with a collection of information if it does not display a currently valid OMB control number. PLEASE DO NOT RETURN YOUR FORM TO THE ABOVE ADDRESS.

0033

1. REPORT DATE (DD-MM-YYYY)	2. REPORT TYPE		3. DATES COVERED (From - To)		
1999-03-01	Final Report		Mar 1, 99 - May 31, 02		
4. TITLE AND SUBTITLE TECHSAT 2) Phased Array Signal Processing			5a. CONTRACT NUMBER 5b. GRANT NUMBER F49620-99-C-0013 5c. PROGRAM ELEMENT NUMBER 5d. PROJECT NUMBER 5e. TASK NUMBER 5f. WORK UNIT NUMBER		
6. AUTHOR(S) Dr. Anthony J. Devaney					
7. PERFORMING ORGANIZATION NAME(S) AND ADDRESS(ES) A. J. Devaney Associates, Inc. 143 Newbury Street- Eighth Floor Boston, MA 02116			8. PERFORMING ORGANIZATION REPORT NUMBER		
9. SPONSORING/MONITORING AGENCY NAME(S) AND ADDRESS(ES) Department of the Air Force Air Force Office of Scientific Research			10. SPONSOR/MONITOR'S ACRONYM(S) 11. SPONSOR/MONITOR'S REPORT NUMBER(S)		
12. DISTRIBUTION/AVAILABILITY STATEMENT Distribution Statement A: Approved for public release. Distribution unlimited					
13. SUPPLEMENTARY NOTES DODAAC CODE: 0EAA7 AFOSR Program Manager: Dr. Arje Nachman					
14. ABSTRACT Tech Sat 21 has, as its goal, the development of a large, sparse, unstructured 3D phased array (Tech Sat 21 array) to be used in orbit above the ionosphere for the surveillance of earth based targets. The key and novel ingredients of the Tech Sat phased array system is that it very sparse and unstructured; i.e. the phased array elements are not rigidly supported and are freely orbiting (uncontrollable) in three-dimensional space. These requirements of the Tech Sat phased array system require that new and novel signal processing algorithms and methods be developed for the surveillance tasks required of the system. The research described herein is directed toward developing such methods and algorithms for the specific tasks of detecting and locating (tracking) moving ground targets (MGT). The approach taken in the project is based on the well-known concept of time-reversal imaging [1, 2, 3] which will be explained in detail in the body of the report. The objectives of the research were to develop the underlying mathematical and physical basis for (computational) time-reversal imaging for time Tech Sat project and to develop and test and evaluate time-reversal based algorithms for MGT detection and tracking.					
15. SUBJECT TERMS					
16. SECURITY CLASSIFICATION OF: a. REPORT		17. LIMITATION OF ABSTRACT		18. NUMBER OF PAGES	
b. ABSTRACT		c. THIS PAGE		19a. NAME OF RESPONSIBLE PERSON Dr. A. J. Devaney	
				19b. TELEPHONE NUMBER (Include area code)	

Final Project Report
Theory and Applications of Computational
Time-reversal Imaging

Anthony J. Devaney
A.J. Devaney Associates, Inc.
143 Newbury Street—eighth floor
Boston, MA 02116

April 11, 2003

20040130 052

Abstract

This document constitutes the final project report for Contract # F49620-99-C-0013 titled *Tech Sat 21 PHASED ARRAY SIGNAL PROCESSING*. The report summarizes the theoretical development of time-reversal based imaging algorithms for locating and tracking ground based targets from multistatic data collected from unstructured phased antenna arrays operating above the ionosphere. The report includes a number of computer simulated examples illustrating the use of the algorithms developed in the project.

Contents

1	Project Summary	2
2	Basic Theory	3
2.1	Born Approximation	4
2.2	Time-reversal Imaging	5
2.3	Transmitter and Receiver Array Point Spread Functions	6
2.4	SVD of the multistatic Matrix	7
2.5	Well-resolved Targets	8
2.6	Non-well resolved Targets and MUSIC	9

3 Near Field Computer Simulations for Tech Sat 21	10
3.1 Computing the multistatic Response Matrix	12
3.2 Computing the Eigenvalues and Eigenvectors of the time-reversal matrix	12
3.3 Forming the conventional time-reversal image	13
3.4 Computing the Pseudo-spectrum	13
3.5 Further Examples	14
4 Tech Sat Simulations	14
4.1 Simulation Results	16
4.2 MUSIC	18
5 Summary	19
6 Table	21
7 References	22
8 Figures	23

1 Project Summary

Tech Sat 21 has, as its goal, the development of a large, sparse, unstructured 3D phased array (Tech Sat 21 array) to be used in orbit above the ionosphere for the surveillance of earth based targets. The key and novel ingredients of the Tech Sat phased array system is that it very sparse and unstructured; i.e., the phased array elements are not rigidly supported and are freely orbiting (uncontrollable) in three-dimensional space. These requirements of the Tech Sat phased array system require that new and novel signal processing algorithms and methods be developed for the surveillance tasks required of the system. The research described herein is directed toward developing such methods and algorithms for the specific tasks of detecting and locating (tracking) moving ground targets (MGT).

The approach taken in the project is based on the well-known concept of *time-reversal imaging* [1, 2, 3] which will be explained in detail in the body of the report. The objectives of the research were to develop the underlying mathematical and physical basis for (computational) time-reversal imaging for the Tech Sat project and to develop and test and evaluate time-reversal based algorithms for MGT detection and tracking. Specific areas addressed in the research included:

- An in-depth investigation of the state-of-the-art of computational time-reversal imaging for three-dimensional (non-planar), non-co-located and sparse phased arrays,
- Development of methods to incorporate models of the ionosphere into the time-reversal based algorithms,

- Incorporation of state-of-the-art signal processing schemes such as *MUSIC*¹ into the time-reversal imaging method,
- Development of methods to reduce the effect of clutter on time-reversal imaging,

The major accomplishments of the project were in the development of a MUSIC algorithm for MGT location and the generalization of the usual and standard methods of time-reversal imaging to non-co-located phased array systems and to non-reciprocal background media such as the ionosphere. All three of these developments have or are in the process of being reported in the literature [4, 5, 6] and could have major impact on the Tech Sat and related projects. In addition to these major results a conceptual scheme for the complete data processing required in the project was developed and a number of computer simulations were completed. These and other results from the project are reported in the body of the report.

2 Basic Theory

In this section we review the revamped theory of computational time reversal imaging developed within the Tech-Sat 21 project. One of the principle goals of the Tech-Sat project is to employ an orbiting set of radar antennas in a *multistatic mode* with the purpose of locating and identifying moving ground targets (MGT's). We can idealize the satellite antenna system as consisting of a phased array system that interrogates a given ground patch containing an MGT as illustrated² in figure 1. In our analysis we will assume a general array consisting of N_r receiving antenna elements and N_t transmitting elements, all of which interrogate a given ground patch that contains a total of M targets. Although the envisioned Tech Sat system will employ co-located transmit and receive antenna elements the generalized theory is necessary to treat non-reciprocal propagation media (such as the ionosphere) and also allows the results obtained in the project to be employed in other Air Force applications (such as imaging of ground targets from phased array antennas deployed on unmanned aerial vehicles (UAV's)). The effective size of the ground patch is determined by the aperture of each antenna element (approximately a meter diameter in Tech-Sat) as well as by Doppler and time-gate processing. The Doppler and time-gate processing are used to reduce the effect of ground clutter and are required pre-processing steps for time-reversal processing to be effective³. We illustrate the Doppler preprocessing steps in figure 2.

The pre-processed data (after clutter reduction) at frequency ω forms an $N_r \times N_t$ matrix that can be expressed in the general form:

$$K_{i,j}(\omega) = \sum_{m=1}^M \int d^3r G(\mathbf{R}_i^r, \mathbf{r}, \omega) O_m(\mathbf{r}, \omega) \psi_j(\mathbf{r}, \omega) \quad (1)$$

¹Standing for MUltiple-Signal Classification.

²All figures appear at the end of the report.

³We will not go into the details of how this processing is done since it is standard radar theory and lies outside of the main goals of the research.

where G is the Green function of the background medium (the atmosphere/ionosphere) and \mathbf{R}_i^r is the location of the i 'th receiving antenna and $\psi_j(\mathbf{r}, \omega)$ is the incident wave generated by the j 'th transmitting antenna. The quantities O_m are the so-called "object profiles" or *scattering potentials* characterizing the ground targets and for penetrable targets are given by an expression of the form:

$$O_m(\mathbf{r}, \omega) = k^2(\mathbf{r}, \omega) - k_0^2(\mathbf{r}, \omega) \quad (2)$$

where $k^2(\mathbf{r}, \omega)$ is the wavenumber of the target and k_0^2 the wavenumber of the background medium. We emphasize that the above model *makes no assumptions about the geometry of the phase array nor of reciprocity of the background medium*. It is also exact within the framework of scalar wave scattering theory.

If we define the column vectors

$$\mathbf{g}_r(\mathbf{r}, \omega) = [G(\mathbf{R}_1^r, \mathbf{r}, \omega), G(\mathbf{R}_2^r, \mathbf{r}, \omega), \dots, G(\mathbf{R}_{N_r}^r, \mathbf{r}, \omega)]^T \quad (3a)$$

$$\psi(\mathbf{r}, \omega) = [\psi_1(\mathbf{r}, \omega), \psi_2(\mathbf{r}, \omega), \dots, \psi_{N_t}(\mathbf{r}, \omega)]^T \quad (3b)$$

we can rewrite Eq.(1) in the symbolic form

$$K(\omega) = \sum_{m=1}^M \int d^3r \mathbf{g}_r(\mathbf{r}, \omega) O_m(\mathbf{r}, \omega) \psi^T(\mathbf{r}, \omega) \quad (4)$$

where the superscript T stands for the transpose operation and where we have used the r subscript on the Green function vector to denote that it corresponds to the receiver array.

The data matrix $K = K_{i,j}$ is called the *multistatic data matrix* and is the key quantity that is employed in many inverse scattering and imaging schemes. In Diffraction tomography (DT) this matrix is used in conjunction with a *slant stacking* algorithm to generate plane wave data which is then input into a *filtered back propagation algorithm* to generate an "image" of the target (the object profiles O_m). Alternatively, the multistatic matrix can be employed to perform time-reversal imaging [1, 2] which is especially useful for locating targets that are small relative to a wavelength, even if the targets are buried in inhomogeneous media whose Green functions are not precisely known. Finally, we mention that conventional SAR imaging does not use the entire multistatic matrix but only its diagonal elements $K_{i,i}$ and is, thus, inherently inferior to the more general schemes, such as time-reversal imaging, that employ the entire matrix.

2.1 Born Approximation

In many cases of interest the effects of the targets on the incident wave field ψ_j are negligible so that ψ_j is, to a good approximation, the wave field that is generated by the j 'th antenna in the background medium without any targets being present. This is called the *Born approximation*⁴ and is employed in the vast majority of imaging and inversion schemes.

⁴More precisely, this is called the *distorted Born approximation* since the background medium is not required to be constant. However, we will interpret the Born approximation within this more general context and not differentiate between uniform (constant) and non-uniform backgrounds except when noted.

Another simplification results in cases where the sensor elements (antennas) are small relative to the wavelength. In this case the incident waves ψ_j are proportional to the Green functions; i.e.,

$$\psi_j(\mathbf{r}, \omega) = C_j G(\mathbf{r}, \mathbf{R}_j^t, \omega)$$

where C_j is a constant (possibly frequency dependent) that we will take to be unity and \mathbf{R}_j^t is the transmitter element location. There is no loss of generality in making this assumption since all sensor array constants can be easily included in the general formalism. Under this assumption, and within the Born approximation, the multistatic response matrix defined in Eq.(4) assumes the form

$$K(\omega) = \sum_{m=1}^M \int d^3r g_r(\mathbf{r}, \omega) O_m(\mathbf{r}, \omega) g_t^T(\mathbf{r}, \omega) \quad (5)$$

where g_r is the Green function vector associated with the receiver array and defined in Eq.(3a) and

$$g_t(\mathbf{r}, \omega) = [G(\mathbf{r}, \mathbf{R}_1^t, \omega), G(\mathbf{r}, \mathbf{R}_2^t, \omega), \dots, G(\mathbf{r}, \mathbf{R}_{N_t}^t, \omega)]^T, \quad (6)$$

is the Green function vector associated with the transmitter array. Physically, each element of g_t is generated by a transmitter antenna point and propagates from that transmitter point into the target region while g_r is generated by a target scattering point and propagates from that target scattering point into the receiving sensor array. This is illustrated in figure 3

From this point on we will employ Eq.(5) as our working definition of the multistatic response matrix. Thus, we will assume that the (distorted wave) Born approximation can be employed and that the incident wave fields generated from the transmitter array are the background Green functions. This second assumption is done only for convenience and can easily be removed. *For the sake of ease of notation we will also suppress the frequency variable ω in all of the following development with the understanding that all equations are in the frequency domain at frequency ω .*

Finally, we emphasize that although we have made the Born approximation we have not required that the Green functions obey a reciprocity condition. For example, even if the transmitters and receivers are co-located (as is presently envisioned for Tech-Sat) we do not require that

$$G(\mathbf{r}, \mathbf{R}_j^t, \omega) = G(\mathbf{R}_j^t, \mathbf{r}, \omega).$$

Thus, the formulation presented here can be employed in both reciprocal and non-reciprocal backgrounds as well as in cases where the transmit and receive arrays are non-co-located.

2.2 Time-reversal Imaging

In the general case where all of the transmitters are simultaneously activated the data measured along the receiver array are given by an expression of the form

$$v = K e$$

where $v = v(\omega)$ is the linear array of output voltages, viewed as an N_r dimensional column vector, measured at the receiver array terminals, $e = e(\omega)$ is the N_t dimensional column vector of applied excitations to the set of transmitting antennas, and K is the $N_r \times N_t$ multistatic matrix. As mentioned earlier we will not explicitly display the frequency variable ω in subsequent equations. In the current theory of time-reversal imaging the object profiles $O_m(\mathbf{r})$ characterizing the targets are assumed to be disjoint profiles, each centered at a spatial location \mathbf{X}_m and each having an effective size that is small relative to the wavelength; i.e.,

$$O_m(\mathbf{r}) = O_m(\mathbf{r} - \mathbf{X}_m). \quad (7)$$

The goal of time-reversal imaging is then to estimate the location \mathbf{X}_m and strength of each scatterer. If we substitute Eq.(7) into Eq.(5) we obtain

$$\begin{aligned} K &= \sum_{m=1}^M \int d^3r g_r(\mathbf{r}) O_m(\mathbf{r} - \mathbf{X}_m) g_t^T(\mathbf{r}) \\ &\approx \sum_{m=1}^M \tau_m g_r(\mathbf{X}_m) g_t^T(\mathbf{X}_m) \end{aligned} \quad (8)$$

where

$$\tau_m = \int d^3r O_m(\mathbf{r}) \quad (9)$$

and where we have made use of the assumption that the targets are small relative to the wavelength. The quantities τ_m thus represent effective *reflection coefficients* for the targets and the goal of time-reversal imaging is then to estimate these reflection coefficients as well as the target locations \mathbf{X}_m .

2.3 Transmitter and Receiver Array Point Spread Functions

Classical coherent imaging from arrays is performed by *back propagating* a coherent wave that is measured across the array into the space from which it propagated. If $\psi(\mathbf{R}^r)$ denotes such a wave measured along the receiver array then the back propagation of ψ is defined mathematically via

$$\chi(\mathbf{r}) = \sum_{j=1}^{N_r} G^*(\mathbf{r}, \mathbf{R}_j^r) \psi(\mathbf{R}_j^r) \quad (10)$$

where χ is the back propagated wave and $\psi(\mathbf{R}_j^r)$ the measured coherent wave across the receiver array. The back propagated wave $\chi(\mathbf{r})$ is the “best” estimate of the measured coherent wave that can be deduced from the measured data.

Now assume that the incident coherent wave to the receiver is the Green function $G(\mathbf{R}^r, \mathbf{X})$ resulting from a source location at \mathbf{X} . We then find using Eq.(10) that the back

propagated field corresponding to the measured Green function is

$$\begin{aligned} H_r(\mathbf{r}, \mathbf{X}) &= \sum_{j=1}^{N_r} G^*(\mathbf{r}, \mathbf{R}_j^r) G(\mathbf{R}_j^r, \mathbf{X}) \\ &= g_r^\dagger(\mathbf{r}) g_r(\mathbf{X}). \end{aligned} \quad (11)$$

The back propagated field H_r is a function both of the field point at which it is evaluated as well as the source point location \mathbf{X} and is the *best image of the source point that can be formed from measurement of the Green function across the receiver array*. This quantity is called the *receiver array coherent point spread function* (PSF). In a similar fashion one can define the transmitter array PSF as

$$H_t(\mathbf{r}, \mathbf{X}) = g_t^\dagger(\mathbf{r}) g_t(\mathbf{X}). \quad (12)$$

We will not digress into the importance and use of the above PSF's at this time but will shortly encounter both of these quantities in connection with time-reversal imaging.

2.4 SVD of the multistatic Matrix

The theory of computational time-reversal imaging depends on the ability to perform a singular value decomposition (SVD) of the multistatic data matrix K . In particular, we consider the singular system

$$K : C^{N_t} \rightarrow C^{N_r} \quad K e_j = \sigma_j v_j \quad (13a)$$

$$K^\dagger : C^{N_r} \rightarrow C^{N_t} \quad K^\dagger v_j = \sigma_j e_j \quad (13b)$$

where j labels the singular system e_j, v_j, σ_j . The normal equations for this system are

$$K^\dagger K e_j = \sigma_j^2 e_j, \quad (14a)$$

$$K K^\dagger v_j = \sigma_j^2 v_j. \quad (14b)$$

The singular vectors $\{e_j\}_{j=1}^{N_t}$ are orthonormal and span the space C^{N_t} while the singular vectors $\{v_j\}_{j=1}^{N_r}$ are orthonormal and span the space C^{N_r} . There are a total of $\min(N_t, N_r)$ singular values $\sigma_j \geq 0$.

In the usual theory of time-reversal imaging [1, 2] where the transmit and receive arrays are coincident the $N_t \times N_t$ matrix

$$T = K^\dagger K \quad (15)$$

is the well-known *time-reversal matrix*. It is seen that in the more general theory developed here that there are, in fact, *two time reversal matrices* $T_1 = K^\dagger K$ as well as $T_2 = K K^\dagger$. T_1 can be considered to be a "conventional" time reversal matrix for a single coincident sensor array identical to the transmit array and T_2 can be considered to be a "conventional" time reversal matrix for a single coincident sensor array identical to the receive array.

If we substitute the expression for the K matrix given in Eq.(8) into Eqs.(13a) and (16b) we obtain

$$\sum_{m=1}^M \tau_m g_r(\mathbf{X}_m) g_t^T(\mathbf{X}_m) e_j = \sigma_j v_j \quad (16a)$$

$$\sum_{m=1}^M \tau_m^* g_t^*(\mathbf{X}_m) g_r^\dagger(\mathbf{X}_m) v_j = \sigma_j e_j \quad (16b)$$

It follows from the above equations that the singular vectors v_j having non-zero singular values are linear combinations of the receiver array Green function vectors $g_r(\mathbf{X}_m)$ while the singular vectors e_j are linear combinations of the complex conjugates of the transmitter array Green function vectors $g_t^*(\mathbf{X}_m)$. If we couple these observations with the fact that the transmit and receiver array Green function vectors are *linearly independent* [4, 5] we conclude that *the vector space spanned by the transmit (receive) Green function vectors is identical to the vector space spanned by the singular vectors e_j^* (v_j) having non-zero singular values σ_j* . These conclusions form the basis for the MUSIC algorithm discussed below.

2.5 Well-resolved Targets

An important special case occurs when the two sets of Green function vectors are orthogonal; i.e., when the following two equations are satisfied:

$$g_r^\dagger(\mathbf{X}_m) g_r(\mathbf{X}_{m'}) = \|g_r(\mathbf{X}_m)\|^2 \delta_{m,m'} \quad (17a)$$

$$g_t^\dagger(\mathbf{X}_m) g_t(\mathbf{X}_{m'}) = \|g_t(\mathbf{X}_m)\|^2 \delta_{m,m'} \quad (17b)$$

where $\delta_{m,m'}$ is the Kronecker delta function and

$$\begin{aligned} \|g_r(\mathbf{X}_m)\|^2 &= g_r^\dagger(\mathbf{X}_m) g_r(\mathbf{X}_m) \\ \|g_t(\mathbf{X}_m)\|^2 &= g_t^\dagger(\mathbf{X}_m) g_t(\mathbf{X}_m) \end{aligned}$$

are the squared norms of the Green function vectors evaluated at the target point \mathbf{X}_m . If Eq.(17a) holds then we say that *the targets are well resolved by the receiver array* while if Eq.(17b) holds we say that *the targets are well resolved by the transmitter array*. When both equations hold then the targets are well resolved with respect to both the transmitter and receiver arrays.

The rational for the above terminology is apparent if we simply note that the inner products in Eqs.(17a) and (17b) are, respectively, the PSF's $H_r(\mathbf{X}_m, \mathbf{X}_{m'})$ and $H_t(\mathbf{X}_m, \mathbf{X}_{m'})$. Thus, for example, the inner product $g_r^\dagger(\mathbf{X}_m) g_r(\mathbf{X}_{m'})$ is *the image of a point target located at $\mathbf{X}_{m'}$ formed at point \mathbf{X}_m by the receiver (receiver) array*. An entirely analogous interpretation can be given the inner product $g_t^\dagger(\mathbf{X}_m) g_t(\mathbf{X}_{m'})$; i.e., as *the image of a point target located at $\mathbf{X}_{m'}$ formed at point \mathbf{X}_m by the transmitter array*. The case of *well resolved targets* thus corresponds to the case where the targets are sufficiently well separated such that the PSF of

either the transmitter or receiver array does not significantly overlap any target other than the one on which it is focused.

For the class of targets that are well-resolved by both the transmit and receive array both Eqs.(17a) and (17b) hold. In this case it is easy to show that *the singular system $\{e_j, v_j, \sigma_j > 0\}$ can be related in a one-to-one manner with the $M \leq \min(N_t, N_r)$ isolated targets*. Indeed, it follows at once from the orthogonality of the Green function vectors that the singular vectors having non-zero singular values for well-resolved targets are given by

$$e_j = \frac{g_t^*(\mathbf{X}_j)}{\|g_t(\mathbf{X}_j)\|} \quad (18a)$$

$$v_j = \frac{g_r(\mathbf{X}_j)}{\|g_r(\mathbf{X}_j)\|} \quad (18b)$$

$$(18c)$$

where $j = 1, 2, \dots, M$. Moreover, the non-zero singular values σ_j are given by

$$\sigma_j = |\tau_j| \|g_t(\mathbf{X}_j)\| \|g_r(\mathbf{X}_j)\| \quad (19)$$

We conclude that *the scatterer strengths are computed directly from the singular values* which, in turn, are readily computed from the measured multistatic data matrix K . Moreover, *the singular vectors give the location of the targets*. Indeed, the coherent image formed using the singular vector e_j will generate the PSF of the transmitter array centered at \mathbf{X}_j while the coherent image formed using the singular vector v_j will generate the PSF of the receiver array centered at \mathbf{X}_j .

2.6 Non-well resolved Targets and MUSIC

One of the primary accomplishments of the Tech-Sat project has been the incorporation of MUSIC into computational time-reversal. MUSIC allows non-well resolved targets to be detected and located. The general idea is that although the set of transmit and receive Green function vectors are not orthogonal in the general non-well resolved case *they are still linearly independent* (This result is proven in [4]) and, as indicated earlier, this implies that *the vector space spanned by the transmit (receive) Green function vectors is identical to the vector space spanned by the singular vectors e_j^* (v_j) having non-zero singular values σ_j* . It then follows that

$$\sum_{\sigma_j=0} e_j^\dagger g_t^*(\mathbf{X}_m) = 0 \quad (20a)$$

$$\sum_{\sigma_j=0} v_j^\dagger g_r(\mathbf{X}_m) = 0 \quad (20b)$$

where the sums are over all singular vectors having zero singular value and where \mathbf{X}_m is any target location. It is important to note that *the above equations hold independent of whether*

the targets are well resolved or not. The orthogonality conditions given in Eqs.(20) is the underlying key to MUSIC. In particular, we introduce the *steering vectors*

$$g_t(\mathbf{X}_p, \omega) = [G(\mathbf{X}_p, \mathbf{R}_1^t, \omega), G(\mathbf{X}_p, \mathbf{R}_2^t, \omega), \dots, G(\mathbf{X}_p, \mathbf{R}_{N_t}^t, \omega)]^T, \quad (21a)$$

$$g_r(\mathbf{X}_p, \omega) = [G(\mathbf{R}_1^r, \mathbf{X}_p, \omega), G(\mathbf{R}_2^r, \mathbf{X}_p, \omega), \dots, G(\mathbf{R}_{N_r}^r, \mathbf{X}_p, \omega)]^T \quad (21b)$$

where \mathbf{X}_p is a *test target location vector* and can assume any value within the region occupied by the targets. It then follows that when the test target location vector coincides with an actual target location; i.e., when $\mathbf{X}_p = \mathbf{X}_m$ then

$$\sum_{\sigma_j=0} e_j^\dagger g_t^*(\mathbf{X}_p) = 0$$

$$\sum_{\sigma_j=0} v_j^\dagger g_r(\mathbf{X}_p) = 0.$$

MUSIC uses the *pseudo-spectrum*

$$\mathcal{P}(\mathbf{X}_p) = \frac{1}{|\sum_{\sigma_j=0} [e_j^\dagger g_t^*(\mathbf{X}_p) + v_j^\dagger g_r(\mathbf{X}_p)]|^2} \quad (22)$$

to determine the target locations. It follows from the analysis presented above that $\mathcal{P}(\mathbf{X}_p)$ will become large (infinity in the ideal case) at all target locations ($\mathbf{X}_p = \mathbf{X}_m$) and will be small otherwise. A number of computer simulated examples of the use of the pseudo-spectrum in the special case where the transmit and receive arrays are co-located are presented in reference [4]. The case of non-co-located arrays are treated in reference [5]. We present simulations for the case of co-located arrays in the following section.

3 Near Field Computer Simulations for Tech Sat 21

We performed a number of computer simulations to test and evaluate the computational time reversal algorithms developed during the course of the project and outlined above. The simplest of these simulations were performed for the case of near field imaging where the objects were located in the near vicinity of the phased array. Although this is not directly relevant to Tech Sat it is relevant to a number of Air Force and DOD applications such as ground imaging from Unmanned Aerial Vehicles (UAV's). These initial simulations also serve as a test of the basic performance of the algorithms in an idealized setting. To avoid discontinuities in the presentation and to avoid confusion we have included all simulation figures at the very end of the document.

The simulations were coded using MATLAB and assume a two-dimensional geometry where the sensor elements are line sources and the targets are line targets all embedded in a homogeneous background and perpendicular to a single plane and all multiple scattering is ignored. From a mathematical point of view we can consider the targets and sensor

elements as points in the two-dimensional space of the plane; i.e., as point locations in R^2 . In the simulations we have limited our attention to the case of co-located arrays which are currently envisioned for Tech Sat. In these cases there is only one Green function vector which we can take to be the transmitter Green function vector g_r defined in Eq.(3a). In the R^2 homogeneous background case the appropriate Green function $G(\mathbf{r}, \mathbf{r}')$ is given by

$$G(\mathbf{r}, \mathbf{r}') = \frac{-i}{4} H_0(k|\mathbf{r} - \mathbf{r}'|) \quad (23)$$

where H_0 is the zero order Hankel function of the first kind. The Green function vectors are then given by

$$\begin{aligned} g_m &= g_r(\mathbf{X}_m) = \{H_0(k|\mathbf{R}_l - \mathbf{X}_m|)\} \\ &= [H_0(k|\mathbf{R}_1 - \mathbf{X}_m|), H_0(k|\mathbf{R}_2 - \mathbf{X}_m|), \dots, H_0(k|\mathbf{R}_N - \mathbf{X}_m|)]^T, \end{aligned} \quad (24)$$

where we have dropped the unessential constant $-i/4$ and where we have denoted the sensor element locations of the phased array by \mathbf{R}_l , $l = 1, 2, \dots, N$. Note that we use the shorthand notation g_m to denote the array Green function vectors g_r evaluated at the scatterer locations \mathbf{X}_m ; i.e., $g_m = g_r(\mathbf{X}_m)$. In terms of the g_r the multistatic response matrix (MSR) K is given by

$$K = \sum_m \tau_m g_m g_m^T. \quad (25)$$

In the simulations we employed a basic image space which is a rectangular grid representing a section of the x, z plane with z being depth (pointing down) and x lateral location (with positive x directed to the right). All dimensions are relative to the wavelength which is taken to be unity. The simulations used an image grid spacing parameter $\delta x = \delta z$ equal to a quarter wavelength $\delta x = \lambda/4$ and an uniformly spaced linear array of from five to nine elements (depending on the simulation) located along the line $z = 0$ and with adjacent sensor element spacing varying from a half-wavelength to up to sixteen wavelengths, again depending on the simulation. We also used from two to four targets located at the same z (depth) coordinate (sixteen wavelengths) but with variable spacing along the x direction. In some of the simulations we added additive noise to the computed multistatic response matrix (MSR matrix) K according to the model

$$\mathcal{K} = K + A e^{i2\pi W} \quad (26)$$

where \mathcal{K} is the noisy MSR matrix, A is an independent Gaussian variable with variance proportional to the peak amplitude of the ideal (computed) MSR matrix K and W is an independent Gaussian variable with unit variance. Thus, the noise model includes both amplitude and phase fluctuations. All parameters used in any given example are listed in the figure captions.

3.1 Computing the multistatic Response Matrix

The multistatic response matrix K is computed using Eq.(25) with the g_m equal to the receiver Green function vectors g_r evaluated at $\mathbf{r} = \mathbf{X}_m$. As an initial example we computed the MSR matrix for the case of two targets ($M = 2$) both located at a depth of sixteen wavelengths for a linear sensor array of nine elements that was centered over the image grid. In this first simulation we used a half-wavelength spacing for the sensor elements, no additive noise, and a target separation of eight wavelengths along the x direction, with one target located exactly at the mid-point of the array and the other displaced by eight wavelengths in the positive x direction. The scattering strengths τ_m of the two targets were equal (to unity). The Coherent Point Spread Function (CPSF) of a regularly spaced sensor array of length a will have an effective lateral width δ at distance z of approximately

$$\delta = z\lambda/a$$

which using $z = 16\lambda$, $a = 4\lambda$ yields $\delta = 4\lambda$. This is equal to half of the spacing between the two targets so this example corresponds to two well-resolved targets.

3.2 Computing the Eigenvalues and Eigenvectors of the time-reversal matrix

The time-reversal matrix T is computed directly from the MSR matrix according to the equation

$$\begin{aligned} T = K^\dagger K &= \sum_m \sum_{m'} \tau_m^* \tau_{m'} g_m^* g_m^\dagger g_{m'} g_{m'}^T \\ &= \sum_m \sum_{m'} \Lambda_{m,m'} g_m^* g_{m'}^T \end{aligned} \quad (27)$$

where

$$\Lambda_{m,m'} = \tau_m^* \tau_{m'} g_m^* g_{m'}.$$

We used a standard eigenvector/eigenvalue solver in MATLAB to compute the eigenvalues and eigenvectors of the time-reversal matrix T in the simulation. Since there are two targets there are two non-zero eigenvalues with associated signal space eigenvectors. We show in Fig. 5 a plot of the eigenvalues and unwrapped phase of the eigenvectors computed from the MSR matrix and for the simulation parameters given above. We see for this case that there are two non-zero eigenvalues corresponding to the two well resolved targets that are separated by eight wavelengths. We also show in the bottom figure the phase of the complex conjugate Green function vectors g_m^* which are seen to be nearly identical (to within an additive integral multiple of 2π) to the phase of the two eigenvectors. This is in agreement with the fact that the complex conjugate of the Green function vectors are proportional to the eigenvectors of the time-reversal matrix in the case of well-resolved targets [4]. We show only the phase of these quantities since the phase of the field is much more important than amplitude (intensity) in imaging and target location estimation.

3.3 Forming the conventional time-reversal image

The time-reversal image is formed using Eq.(10). For the well resolved target case the image field $\psi_m(\mathbf{r})$ is proportional to the Coherent Point Spread Function (CPSF) of the sensor array. This is well approximated in the first simulation where the targets are separated by 8λ . The magnitude of the focused fields from the two eigenvectors for this case (whose phases are shown in Fig. 5) are shown in Fig. 6. We have superimposed an X at the actual target locations to show that the image fields tend to peak in the vicinity of the targets. We have also shown for comparison the magnitude of the fields generated from the complex conjugate Green function vectors g_m^* which are the eigenvectors in the ideal case where the targets are perfectly resolved and whose phase distributions along the sensor elements are also shown in Fig. 5. It is clear from the figure that the image intensities for both the imaged eigenvectors and the imaged Green function vectors are very close as can also be inferred from the fact that their phase distributions along the sensor elements are almost identical as shown in Fig. 5.

It is clear from Fig. 6 that the images generated from the eigenvectors of the time-reversal matrix provide a good indicator of the target locations. The reasons for this are that the targets are well-resolved so that their separate image fields do not overlap significantly. However, we will see later examples where the targets are not well-resolved so that the images generated by the eigenvectors of the time-reversal matrix do not provide good indication of the target locations. Moreover, even in this example where the targets are well separated the depth resolution generated by the classical time-reversal images is not very good. Indeed, a close inspection of the images in Fig. 3 shows that the maximums do not occur at the target locations but rather in the immediate vicinity of the array (see gray scale bar). The reason for this is that, as was mentioned earlier, the longitudinal resolution associated with the CPSF is much less than is the horizontal resolution: a fact that is clear from Fig. 6.

3.4 Computing the Pseudo-spectrum

The MUSIC algorithm was implemented using Eq.(22) with the denominator computed using two different methods that are described in [4]. Note that in this case where the transmitters and receivers are co-located that the pseudo-spectrum reduces to the simplified form

$$\mathcal{P}(\mathbf{X}_p) = \frac{1}{|\sum_{\sigma_j=0} |e_j^\dagger g_p^*|^2|}$$

where $g_p = g_m|_{m=p} = g_r(\mathbf{X}_p)$ with \mathbf{X}_p equal to the location of a test target. In all of the simulations the two methods of computing the denominator gave essentially equivalent results so we only show the result obtained by the direct method of projecting g_p onto the noise subspace. In the first simulation discussed so far the targets are well-resolved so that each eigenvector is associated with one of the two targets and the conventional method of imaging the eigenvectors illustrated in Fig. 6 gives good indication of target location, at least as regards the lateral (x) location. The computed pseudo-spectrum for this example is shown

in Fig. 7 while Fig. 8 shows the pseudo-spectrum superposed on top of the conventional time-reversal images. Also shown in text are the estimates of target location obtained by simply finding the maximum of the pseudo-spectrum. As expected in the absence of noise perfect target location estimation is obtained.

3.5 Further Examples

As a second example we repeated the first simulation but added noise equal to 20% of the peak value of the magnitude of the (noise free) MSR matrix and also increased the spacing between adjacent sensor elements to two wavelengths. In Fig. 9 we show the plot of the eigenvalues as well as the phase of the eigenvectors and complex conjugate Green functions. Note that the noise has the effect of adding non-zero eigenvalues beyond the first two dominant ones. Also note that the phases of the conjugate Green functions are no longer equal to the phases of the first two eigenvectors due to the effect of the increased sensor separation and also the additive noise. In Fig. 10 we show the images generated from the two dominant eigenvectors together with those generated using the complex conjugate Green function vectors. It is seen that these images possess a complicated spatial structure with multiple lobes making it difficult to locate the two targets. In Fig. 11 we show the pseudo-spectrum which, although noisy, returns exact estimates of the target locations.

4 Tech Sat Simulations

The Tech-Sat simulations included the presence of the ionosphere and are also performed in the far field of the targets. Both of these aspects of the problem complicate the imaging problem and the simulations of the time-reversal based imaging algorithms discussed in the report. As in the near field simulations presented in the previous section we consider the simplified case of two space dimensions where the horizontal x axis is parallel to the locally flat earth surface and the vertical z axis has its origin at a height h above the earth with positive z pointing downward. A phased antenna array consisting of N antenna elements each with a uniform aperture of diameter d is assumed to be deployed along the x axis at $z = 0$ (at a height h above the earth surface). Intervening between the phased antenna array and the earth is the ionosphere which is modeled as a thin phase screen located at altitude l above the earth. The thin phase screen model is illustrated in fig. 4. The objective of the simulation is to illustrate the use of the time-reversal based processing schemes outlined in the previous sections of the report for locating one or more moving ground targets (MGT) from the multistatic data matrix acquired at a single frequency by the orbiting array. We will assume that all data collection is performed over a short period of time in which everything is "frozen" so that variations in antenna location, target location, ionosphere parameters, etc. can be ignored. The assumption of a frozen background and data acquisition system is reasonable within the context of Tech Sat due to the planned use of frequency multiplexing in the acquisition of the multistatic data matrix. Thus, in particular, this quantity will be

obtained by simultaneously exciting orthogonal signals at all the transmitter locations and not by sequentially exciting the transmitter elements in time.

We will take the nominal altitude h of the Tech Sat array to be 400 kilometers (km) and place the thin phase screen model of the ionosphere at $l = h/2 = 200$ km. The wavelength of the radiation is taken to be $1 \text{ cm} = 10^{-2} \text{ m}$ and we will assume that the array consists of $N = 5$ antennas aligned along the x axis at $z = 0$ (height h) and each of which has an effective aperture diameter of one meter. Due to the large propagation distances and short wavelength we can employ the following Fraunhofer approximation for the field radiated above the ionosphere by an antenna element located at $\alpha_k = (x = x_k, z = 0)$:

$$\Phi(\mathbf{r}, \alpha_k) = \sqrt{\frac{k_0}{2\pi}} \frac{e^{i(kz - \frac{\pi}{4})}}{\sqrt{z}} e^{i\frac{k_0}{2z}(x - x_k)^2} \text{sinc} \left[\frac{d}{\lambda z} (x - x_k) \right], \quad (28a)$$

where $k_0 = 2\pi/\lambda$ is the free space wavenumber and

$$\text{sinc}(x) = \frac{\sin \pi x}{\pi x}$$

is the sinc function. The field Φ is radiated from each antenna element down to the thin phase screen where it is spatially modulated by a transmission function of the general form

$$T(x) = e^{i\pi A_0 \sin(\frac{2\pi}{L_0} x)}$$

where the amplitude A_0 and period L_0 are parameters of the thin phase screen model. In the simulations we took $A_0 = 1$ and $L_0 = 30$ m. More general models for the phase screen can be employed and are easily incorporated into the Matlab code which is available from the author's web site.

The thin phase screen transmission function $T(x)$ multiplies the antenna field $\Phi(\mathbf{r}, \alpha_k)$ at $z = l = h/2 = 200$ m to generate the boundary value field $\chi(\mathbf{r}, \alpha_k) = T(x)\Phi(\mathbf{r}, \alpha_k)$ which is then propagated to ground using a discretized Kirchoff approximation

$$\Phi(\mathbf{r}, \alpha_k) = \delta x \sum_{j=-J}^J \chi(\mathbf{r}_j, \alpha_k) \sqrt{\frac{k_0}{2\pi}} \frac{e^{i(k_0 \Delta z - \frac{\pi}{4})}}{\sqrt{\Delta z}} e^{i\frac{k_0}{2\Delta z}(x - x_j)^2} \text{sinc} \left[\frac{\delta x}{\lambda \Delta z} (x - x_j) \right] \quad (28b)$$

where $\chi(\mathbf{r}_j, \alpha_k)$ are the sample values of the boundary value field at the sample points $\mathbf{r}_j = (j\delta x, l)$, $\Delta z = z - l$ is the propagation distance from the phase screen and the maximum index J is selected large enough to encompass the major lobe of the radiation pattern from each antenna element. Eq.(28b) can be regarded to be a superposition of the fields generated by a linear array of adjacent small antenna elements having diameters δx and boundary value fields $\chi(\mathbf{r}_j, \alpha_k)$. In the simulations we took $\delta x = d = 1$ m since the distance of the phase screen from the phased array was sufficiently large that this value of δx was well below the required Nyquist sampling interval.

$\Phi(\mathbf{r}, \alpha_k)$ is the total field radiated by an antenna centered at α_k in the presence of the thin phase screen⁵. We will also have need of the wavefield $\Psi(\alpha_k, \mathbf{x}_m)$ which is the output

⁵We assume that reflections by the ionosphere can be ignored or time gated out by the Tech Sat antenna elements so that the reflected wave component of Φ is effectively zero.

from the k antenna element due to a point source located on the ground at \mathbf{x}_m . This field is computed using the model Eq.(28a) for the up going wave from a source point at \mathbf{x}_m and then the Kirchoff model Eq.(28b) for propagation up to the antenna element located at α_k . However, due to reciprocity, it is easily verified that⁶

$$\Psi(\alpha_k, \mathbf{x}_m) = \Phi(\mathbf{x}_m, \alpha_k). \quad (29)$$

The field $\Phi(\mathbf{r}, \alpha_k)$ plays the role of the Green function $G(\mathbf{r}, \alpha_k)$. In place of the Green function vector we now have the “antenna vector”

$$\phi(\mathbf{r}) = [\Phi(\mathbf{r}, \alpha_1), \Phi(\mathbf{r}, \alpha_2), \dots, \Phi(\mathbf{r}, \alpha_N)]^T, \quad (30a)$$

where Φ is defined in Eqs.(28). The multistatic data matrix is given by

$$K = \sum_{m=1}^M \tau_m \phi(\mathbf{x}_m) \phi^T(\mathbf{x}_m), \quad (30b)$$

which follows at once from the reciprocity condition Eq.(29).

In some of the simulations uncorrelated noise was added to the output from the antenna elements according to the model

$$\hat{K}_{j,k} = K_{j,k} + A_1 \exp ix_{j,k}$$

where \hat{K} is the noisy matrix and A_1 is a real constant which we took to be either zero or 0.1 times the maximum value of the noise free K matrix. The quantity $x_{j,k}$ is a zero mean, uncorrelated and uniformly distributed random matrix over $[-\pi, \pi]$. We note that the assumption of point targets is very reasonable in the current application in view of the very large propagation distances involved even though the wavelength is quite small. In particular, the incident field $\Phi(\mathbf{r}, \alpha_k)$ from each antenna element evaluated on the ground will be effectively plane over any reasonably sized ground vehicle with the result that the point scattering model underlying the analysis presented in the paper should be valid.

4.1 Simulation Results

The Matlab code *ap01.m* essentially tests the forward simulation model Eqs.(28). Among other computations, this code computes the field intensity over the earth surface ($z=400$ km) with and without the presence of the phase screen. An example is presented in fig.12 which shows the field intensity at the top of the phase screen as well as over the ground with and without the phase screen being present. The parameter values for this simulation, and all other simulation examples, are given in Table 1. In this example we have used a uniform linear array of $N = 5$ elements equally spaced over a half kilometer and all of which

⁶In all the Matlab codes discussed later and used in the simulations the up going wave field Ψ is actually computed using Eqs.(28) and the reciprocity condition can, in fact, be verified using these codes.

were simultaneously excited by unit amplitude, in-phase pulses to simulate a plane wave propagating parallel to the z axis. The middle and top plots in the figure clearly show the grating lobes that are generated for this case. The grating lobe periods are given in the table where the first number is for the top of the phase screen and the second for the earth surface. It is also apparent from the bottom plot that the grating lobes are randomized due to the presence of the phase screen. The code *ap01.m* can also be used to test the accuracy of the simple Kirchoff model Eq.(28b) for generating the incident field below the phase screen. In particular, the reader can verify using the code that the field amplitude on the earth surface obtained using the direct model Eq.(28a) with $z = 400$ km. agrees closely with the field amplitude computed using the composite model Eq.(28b) with the phase screen amplitude A_0 set equal to zero; i.e., with $T(x) = 1$.

The code *ap02.m* allows the user to use up to five targets distributed over a half kilometer on the earth surface and computes the multistatic data matrix K and the eigenvectors and eigenvalues of the time-reversal matrix $T = K^*K$. These eigenvectors are equal to the singular vectors $v_j = u_j^*$ that are used in the computation of the classical time-reversal image field via the process of back propagation as discussed earlier in the report. For the case of a single target or a set of "well resolved targets" the time-reversed image field is the PSF of the antenna array centered at the target(s) locations. As discussed earlier the PSF yields the "best" image of the target location that can be generated from the observed data (the K matrix).

We show in fig. 13 plots of the intensity of the time-reversed field over the ground for a single target located at the center $x_m = 0$ of a half kilometer of image space using the same set of parameters employed in the first example. The figure shows the results for three cases: (i) when no phase screen is present, (ii) when a phase screen is present and (iii) when a phase screen is present but the image field is generated by using the free space model Eq.(28a). All three cases were computed by first generating the K matrix and then back propagating the eigenvector corresponding to the largest eigenvalue. The third case corresponds to using the free space antenna vector generated using the free space propagation model Eq.(28a) with $z = 400$ km in the computation of the image field and is of interest due to the fact that an adequate model of the thin phase screen (the background Green function) may not be available. Thus, although the exact eigenvector of the K matrix can be computed the step of image formation via back propagation may not be exactly implementable due to imperfect knowledge of the background Green function. As indicated in the figure the use of free space back propagation shifts the location of the target but does, nevertheless, give a rough estimate of its position.

We show in fig. 14 results for the case of an irregular (unstructured) antenna array having center locations as indicated in Table 1. We have again used a single target located at the center $x_m = 0$ and again show the three cases of no phase screen, phase screen, and phase screen data but free space back propagation. Note the elongated period in the grating lobe structure compared with that displayed in fig 13 due to the smaller minimum separation of antenna elements of the phased array.

It is apparent from figures 13 and 14 that the conventional time reversed image field yields

good estimates of the target location in the absence of noise and clutter if the background Green function (or antenna vector) is known and fair estimates if this quantity is not known and free space back propagation is employed. In fig 15 we show the effect of multiple targets (clutter) on the image formation process. This example was generated with a phase screen present using the code *ap03.m* and the parameters given in Table 1. The example used three targets having equal scattering strengths $\tau_m = 1$ located at $x_m = -200, 0$, and $+100$ meters and illustrates the difficulty of associating individual targets from the raw back propagated images even in the absence of additive noise. The problem is exacerbated in the absence of the phase screen where the grating lobes make target location even more difficult.

4.2 MUSIC

The Matlab code *ap04.m* implements the MUSIC algorithm. We applied this code to the same target and antenna geometry employed in the example given in fig. 15 and present the results in figs. 16 and 17. The results shown in fig. 16 correspond to no phase screen with the top plot being the pseudo-spectrum for the no noise case and the bottom for an additive noise having an amplitude coefficient $A_1 = .1$ corresponding to a signal to noise ratio $\max K / \max W$ of ten where W is the additive noise term. This same noise amplitude and signal to noise ratio was employed in all of the simulations having noise present. As mentioned in our discussion on grating lobes the multistatic data matrix is not exactly periodic due to its dependence on the square x_m^2 of the target's location so that in the absence of noise it should be possible to perfectly locate a target even in the presence of these lobes. Although this is not easily accomplished by direct viewing of the classical time-reversed (back propagated) image fields the target locations are immediately and automatically generated by the pseudo-spectrum as is apparent from the top plot in fig. 16. However, when even a small amount of noise is added a number of false peaks in the pseudo-spectrum appear that are due both to additional clutter like singular vectors in the noise subspace \mathcal{N} as well as to the basic ill-posedness of the inverse problem in the presence of the grating lobes. This is illustrated in the bottom of the figure where a small amount of additive noise with the noise amplitude coefficient $A_1 = .1$ has been added.

In fig. 17 we show the results obtained for the same set of simulation parameters used for fig. 16 but with a phase screen present. The randomizing effect of the presence of the phase screen on the grating lobes is apparent from the bottom plot which, on comparison, with the bottom plot of fig. 17 is seen to yield much more robust estimates of the target locations. We performed the same simulation but used the free space steering vector and show the results in fig. 18. It is seen that the free space steering vector does not give accurate estimates of target location but does, nevertheless yield estimates that are in the general ball park of the correct locations.

The final example presented in fig. 19 is of two close targets in the presence of clutter and additive noise. This example is important since actual field data will contain a number of clutter targets as well as noise. Both examples assumed the presence of a phase screen with the top plot corresponding to the no noise case while the bottom plot included an

additive noise with noise amplitude $A_1 = .1$. The two plots clearly show the robustness of the MUSIC algorithm and also indicate its ability to “super-resolve” close targets that would not be resolvable using standard field back propagation. Indeed, the two dominant targets in this example are separated by five meters which is roughly equal to the classical resolution $\Delta = \lambda h/.5 = 4$ m of a densely packed, uniform antenna array one-half kilometer in length.

5 Summary

This project had as its primary goal the development of theory and associated algorithms for locating ground based targets using the proposed Tech sat phased array antenna system. To this end a theory based on classical time-reversal imaging [1, 2] was developed and coded in Matlab based algorithms. The basic theory has been submitted for publication [4, 5, 6] and is summarized in this final project report. The developed theory is applicable to Tech Sat as well as to general problems that require imaging of targets obscured by an inhomogeneous background medium such as the ionosphere or foliage.

The theory and algorithms developed in the project assume measurement of the multi-static data matrix $K = \{K_{j,k}\}$ at a single temporal frequency ω by a phased array antenna and uses the SVD of this matrix as well as the Green function of the background medium to generate images of the target locations. Two methods of image generation from the multi-static data were developed and tested in computer simulations: (i) image formation via the classical method of time-reversal (or field back propagation) imaging [2] and (ii) use of the MUSIC pseudo-spectrum to form the images [4, 5, 6]. Both of these methods use the singular vectors in the SVD of the K matrix where, however, the classical time-reversal scheme uses those vectors associated to the dominant singular values while the MUSIC method employs those singular vectors associated to the small singular values. It was shown and demonstrated via computer simulation that the classical method works well in cases of a few well separated targets (well resolved targets) but fails if the number of targets is large or they are closely located. On the other-hand the MUSIC method works independent of these assumptions and returns “super-resolution” estimates of the target location that are far better than would be obtained via the classical time-reversal based imaging method.

The current final project report included a discussion of the effects of grating lobes, clutter and additive noise on the image formation process. It was argued and later demonstrated in the computer simulations that the presence of a inhomogeneous medium between the phased array antenna and the targets can significantly reduce the grating lobes and increase the performance of the algorithms. Although earlier studies [7] have shown that the presence of such a background can increase the resolution of the time-reversal imaging process the effect demonstrated here appears to be different and is simply due to the randomizing of the grating lobes of the antenna radiation pattern and not due to an effective increase of the aperture of the antenna array. A simulation of the performance of the MUSIC algorithm in the presence of two adjacent and dominant targets and a number of clutter targets and additive noise was presented and illustrated the robustness and super-resolution ability of the algorithm.

Both the classical time-reversal imaging scheme as well as the MUSIC algorithm require knowledge of the background Green function. In the Tech Sat simulations the background was modeled as a thin phase screen and simulations were performed for cases where this background was known and also for cases where the free space background Green functions were employed in the image formation process. The simulations indicate that excellent results are obtained when the correct Green function is employed in the image formation process but that performance degraded in some cases significantly when the back propagation or MUSIC algorithms were implemented using the free space Green function. An important avenue for research is the estimation of the background from the multistatic data and also from ancillary data obtained using, for example, the phased array antenna but other emission sources such as are employed in Silent Sentry and similar projects. Within the context of the Tech Sat project we mention, for example, that the reflections off the ionosphere which are assumed time-gated out in the simulations presented here can be used to form an estimate of the index of refraction distribution of this medium which can then be employed to generate an estimated background Green function. An inversion algorithm based on the distorted wave Born approximation has been recently developed [8] for precisely such cases and will be integrated into the time-reversal based schemes discussed here in the future.

6 Table

figure	code	α_k in m.	x_m in m.	τ_m	L
1	ap01.m	-206,-104,-1,101,203	-	-	20, 40
2	ap02.m	-206,-104,-1,101,203	0	1	40
3	ap02.m	-155,-104,50,75,153	0	1	156
4	ap03.m	-155,-104,50,75,153	-201,-1,99	1,1,1	156
5	ap04.m	-155,-104,50,75,153	-201,-1,99	1,1,1	156
6	ap04.m	-155,-104,50,75,153	-201,-1,99	1,1,1	156
7	ap04.m	-155,-104,50,75,153	-201,-1,99	1,1,1	156
8	ap04.m	-155,-104,50,75,153	-201,-126,-101,-96,-1,3,49,99	.1,.1,1,1,.1,.1,1,1,1,1	156

Table 1: Parameters used in the simulations

7 References

References

- [1] C. Prada, J.L. Thomas and M. Fink, "The iterative time reversal process: Analysis of the convergence", *Journal of the Acoustical Society of America*, **97**, pp.62-71 (1995).
- [2] C. Prada, S. Manneville, D. Spoliansky and M. Fink, "Decomposition of the time reversal operator: Detection and selective focusing on two scatterers", *Journal of the Acoustical Society of America*, **99**, pp.2067-2076 (1996).
- [3] R.K. Snieder and J.A. Scales, "Time-reversed imaging as a diagnostic of wave and particle chaos," *Physical Review E*, **58**, pp.5668-5675 (1998).
- [4] A.J. Devaney, "Super-resolution processing of multistatic data using time-reversal and MUSIC", paper accepted for publication in the *Journal of the Acoustical Society of America*.
- [5] S. Lehman and A.J. Devaney, "Transmission Mode Time-Reversal Imaging with MUSIC", paper to appear May, 2003 in the *Journal of the Acoustical Society of America*.
- [6] A.J. Devaney, "Time Reversal Imaging of Obscured Targets From Multistatic Data", paper submitted for publication in *IEEE Transactions of Antennas and Propagation*.
- [7] N. Mordant, C. Prada, and M. Fink, "Highly resolved detection and selective focusing in a waveguide", *Journal of the Acoustical Society of America*, **105**, pp.2634-2642 (1999).
- [8] A.J. Devaney and M. Dennison, "Inverse scattering in inhomogeneous background media", *Inverse Problems*, submitted for publication, Preprint available on the author's web site.

8 Figures

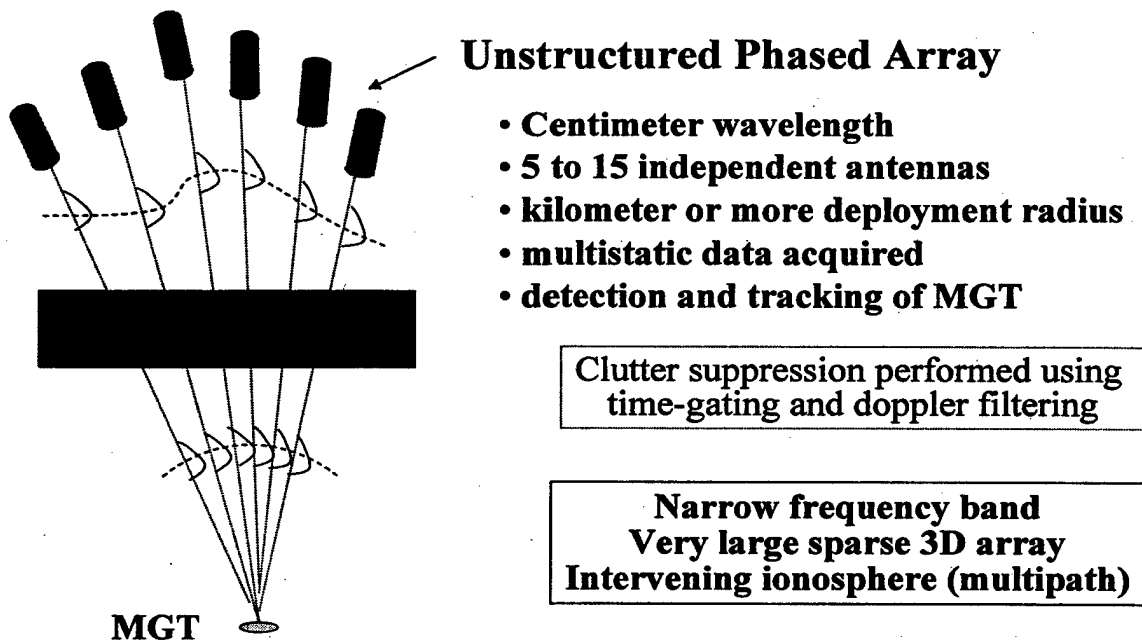


Figure 1: Illustration of the Tech Sat phased array system for MGT detection and tracking

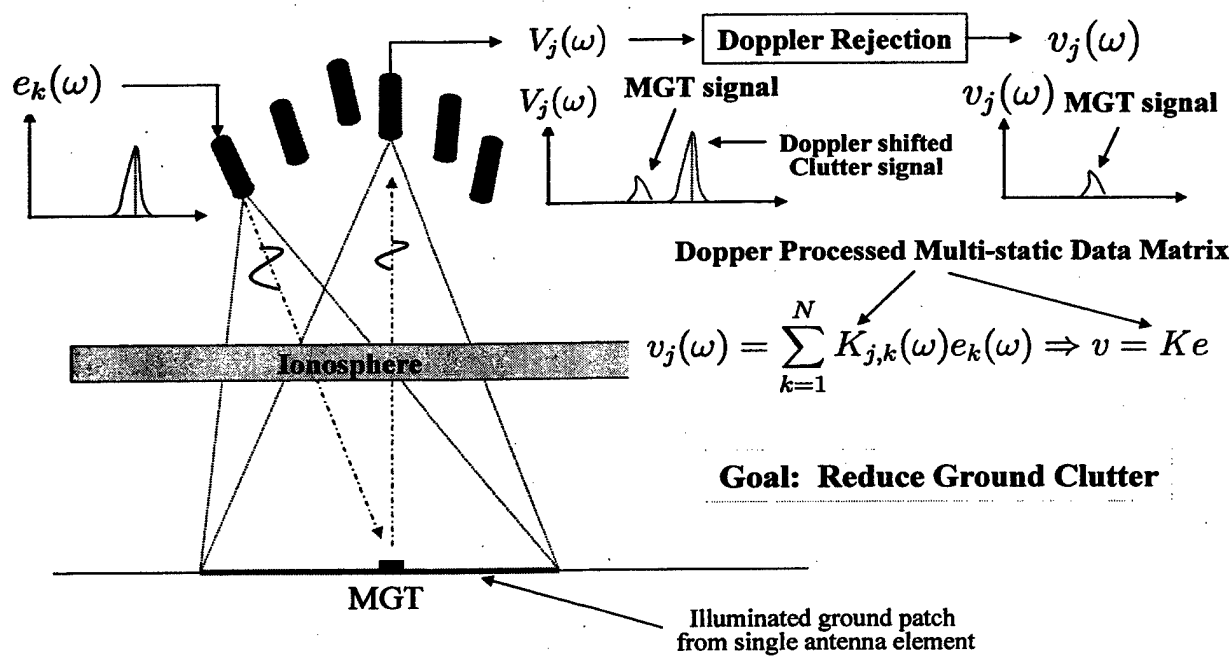


Figure 2: Doppler and time-gating are used to reduce the size of the ground patch and thus reduce clutter. In this figure an exciting voltage $e_k(\omega)$ is applied to a transmitting antenna element and the reflected signal from the target generates the voltage $V_j(\omega)$ at a receiving element. This received voltage is input to a Doppler rejection filter to generate the clutter reduced signal $v_j(\omega)$.

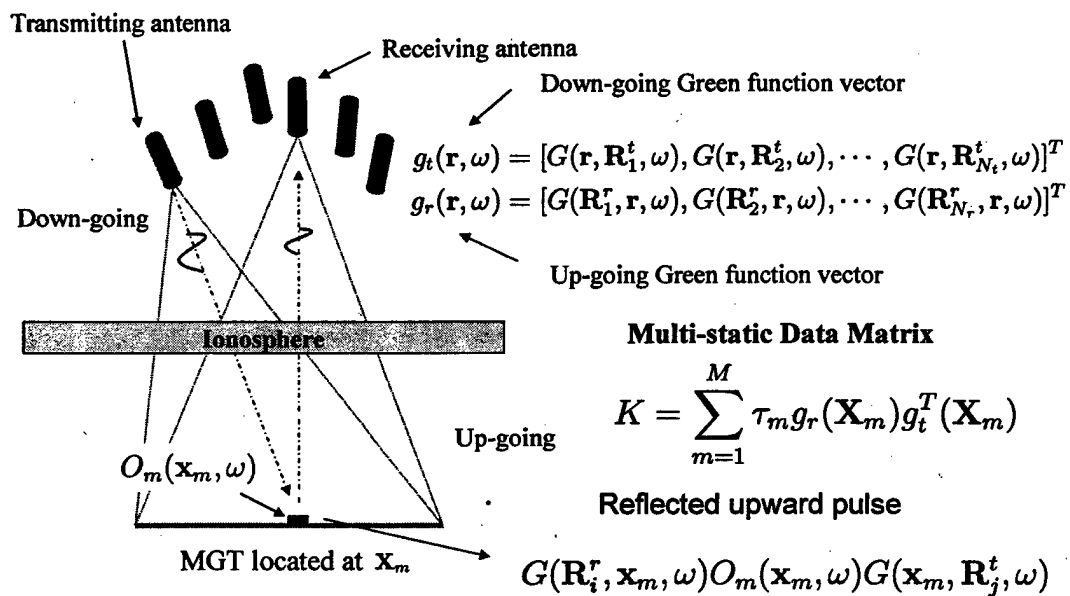
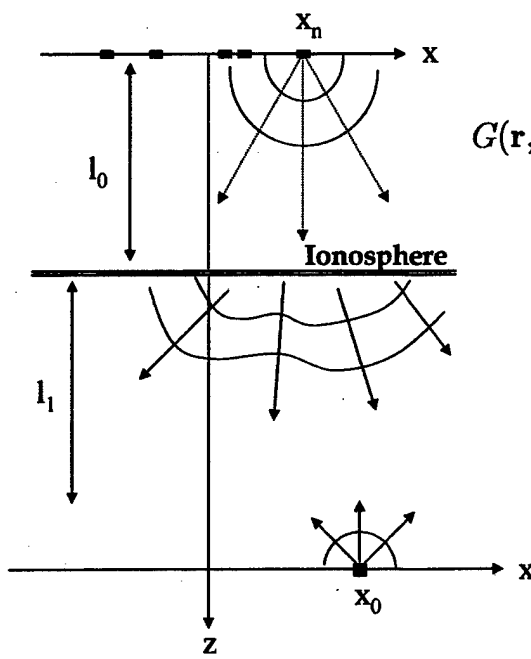


Figure 3: Within the Born approximation the multistatic data matrix K can be expressed as the sum of outer products of transmitter (down going) g_t and receiver (up going) g_r Green function vectors. The τ_m are the effective target reflection coefficients.

Computer Simulation Model



Fresnel Approximation

$$G(\mathbf{r}, \mathbf{r}_n) = \sqrt{\frac{k}{2\pi}} \frac{e^{i(kz - \frac{\pi}{4})}}{\sqrt{z}} e^{ik\frac{(x - x_n)^2}{2z}} \text{sinc}[\frac{d}{\lambda z}(x - x_n)]$$

Thin phase screen model

$$T(x) = \exp[i2\pi A_0 f(x)]; \quad f(x) = \sin\left(\frac{2\pi}{L}x\right);$$

Down-going wave

$$U_-(\mathbf{r}, \mathbf{r}_n) = \delta x \sum_{j=1}^{N_a} T(x_j) G(\mathbf{r}_j, \mathbf{r}_n) G(\mathbf{r}, \mathbf{r}_j)$$

Up-going wave

$$U_+(\mathbf{r}, \mathbf{r}_n) = \delta x \sum_{j=1}^{N_a} R(x_j) U_-(\mathbf{r}_j, \mathbf{r}_n) G(\mathbf{r}, \mathbf{r}_j)$$

Figure 4: A thin phase screen model is used to simulate the effect of the ionosphere. This model can also be the basis for a parameterized model for the background Green function vectors. In the figure the quantities T and R are the transmission and reflection coefficients of the thin phase screen model and, as a first approximation, are given by a sinusoidal model.

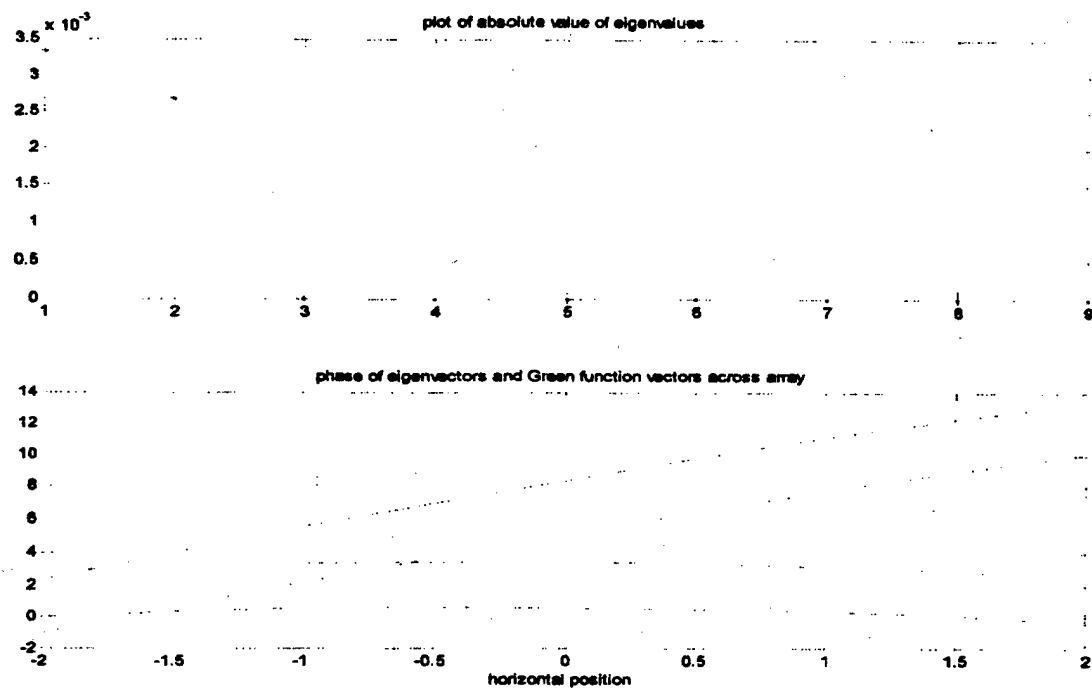


Figure 5: (Top) Plot of the magnitude of the eigenvalues of the time-reversal matrix. (Bottom) plots of the (real) phase of the two eigenvectors corresponding to the two non-zero eigenvalues (solid) and of the phase of the complex conjugate of the two Green function vectors (dashed).

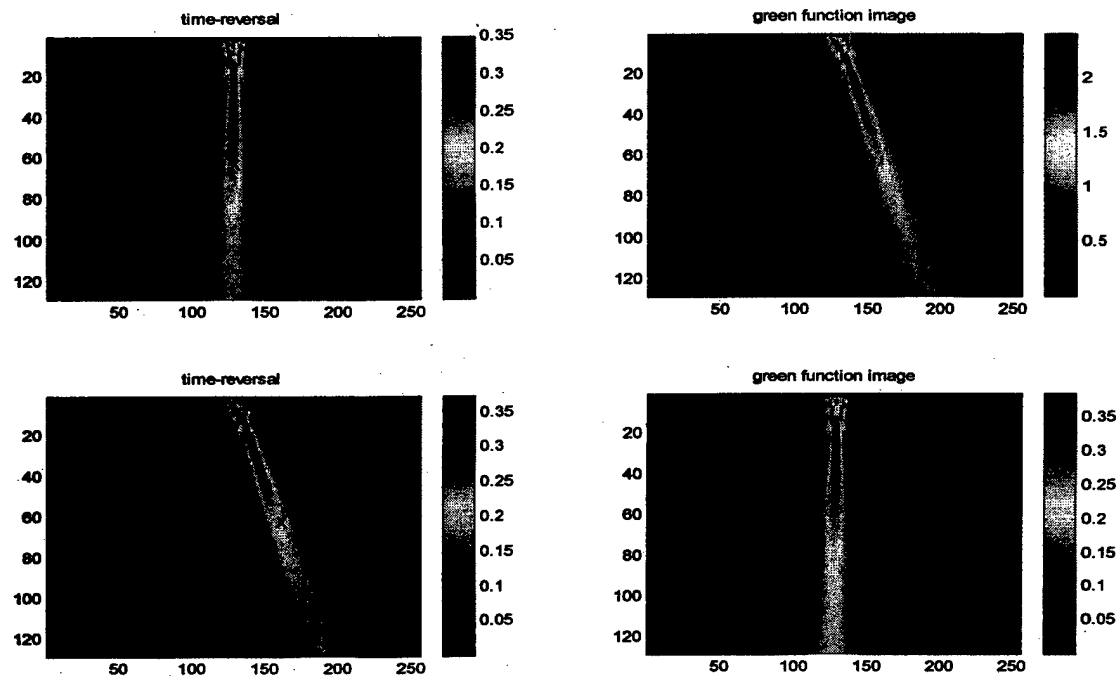


Figure 6: (Left) Images generated by the two eigenvectors shown in Fig. 5 and (right) images generated by the complex conjugate Green function vectors shown in Fig. 5. The “X” on the images indicates the location of the targets.

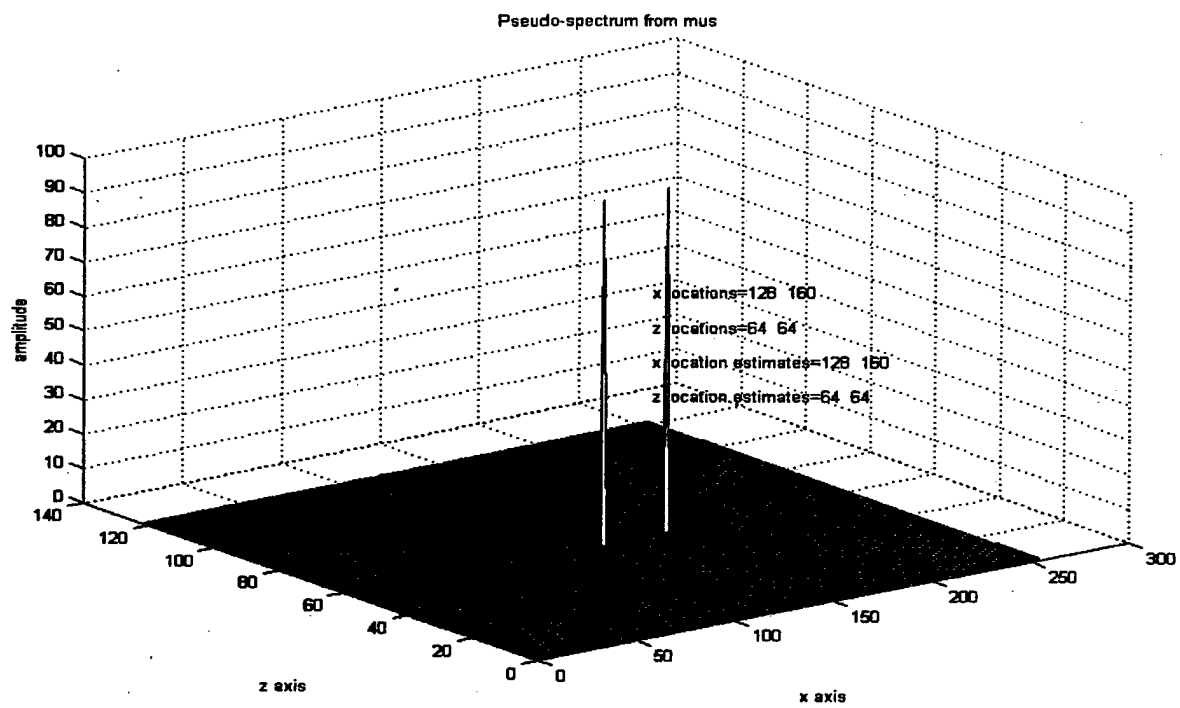


Figure 7: The pseudo-spectrum computed for the simulation depicted in Fig. 6. The peak values of the pseudo-spectrum are given as text in the figure and indicate that exact results were obtained for both the x and z location estimates.

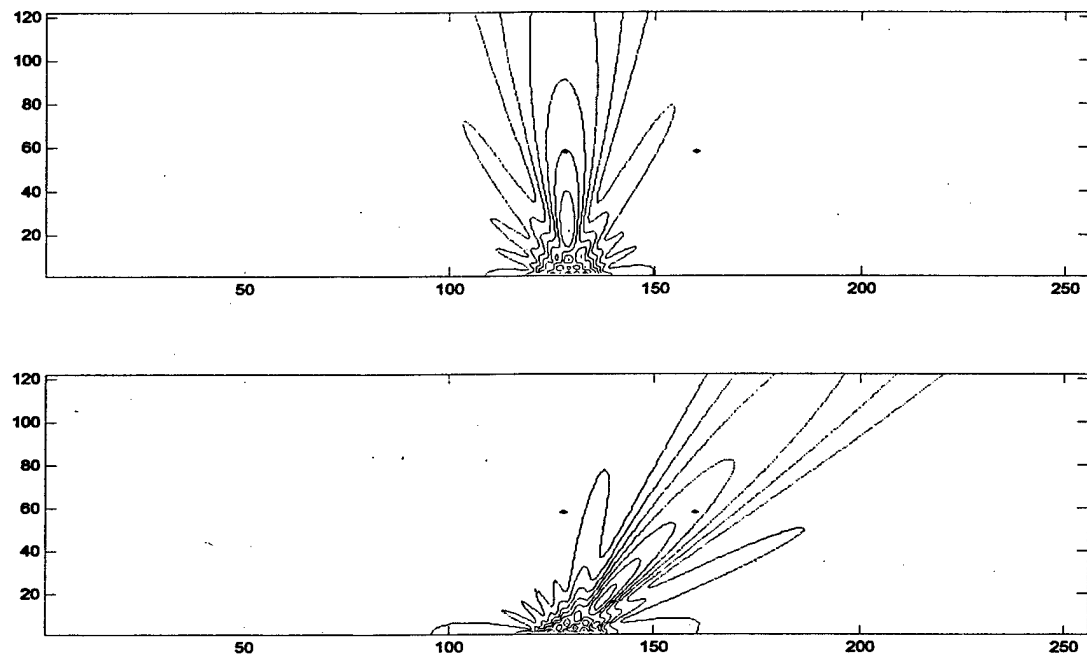


Figure 8: Contour plots of the time-reversal images shown in Fig. 6 on which are superposed the pseudo-spectrums shown in Fig. 7.

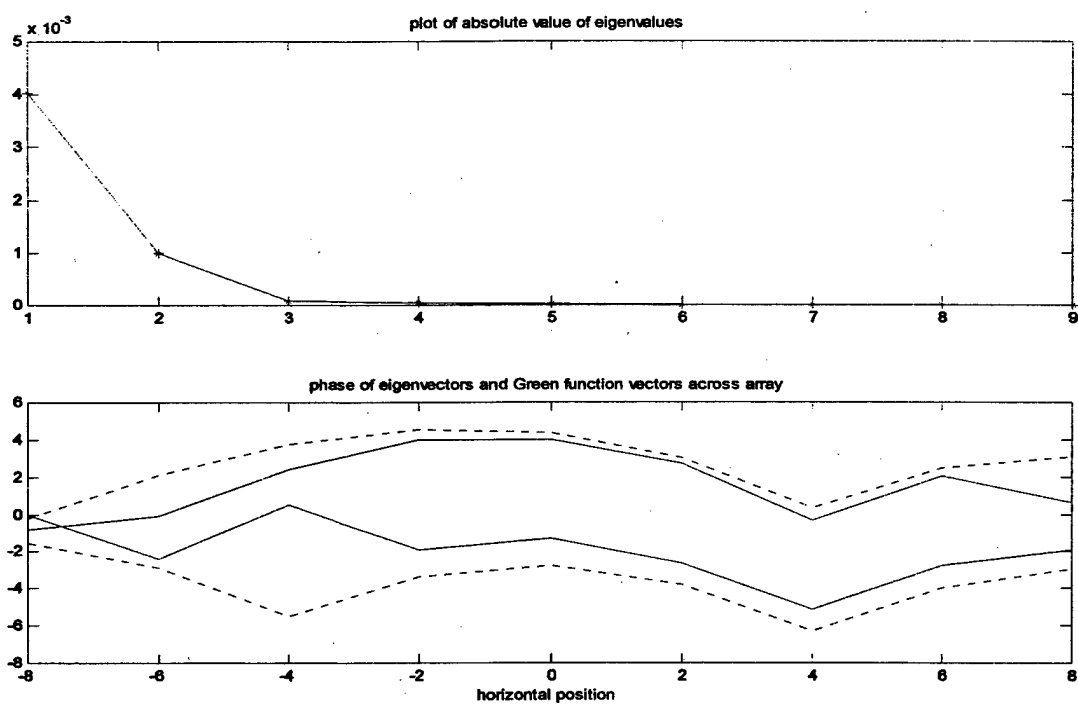


Figure 9: (Top) Plot of the magnitude of the eigenvalues of the time-reversal matrix. (Bottom) plots of the (real) phase of the two eigenvectors corresponding to the two non-zero eigenvalues (solid) and of the phase of the complex conjugate of the two Green function vectors (dashed).

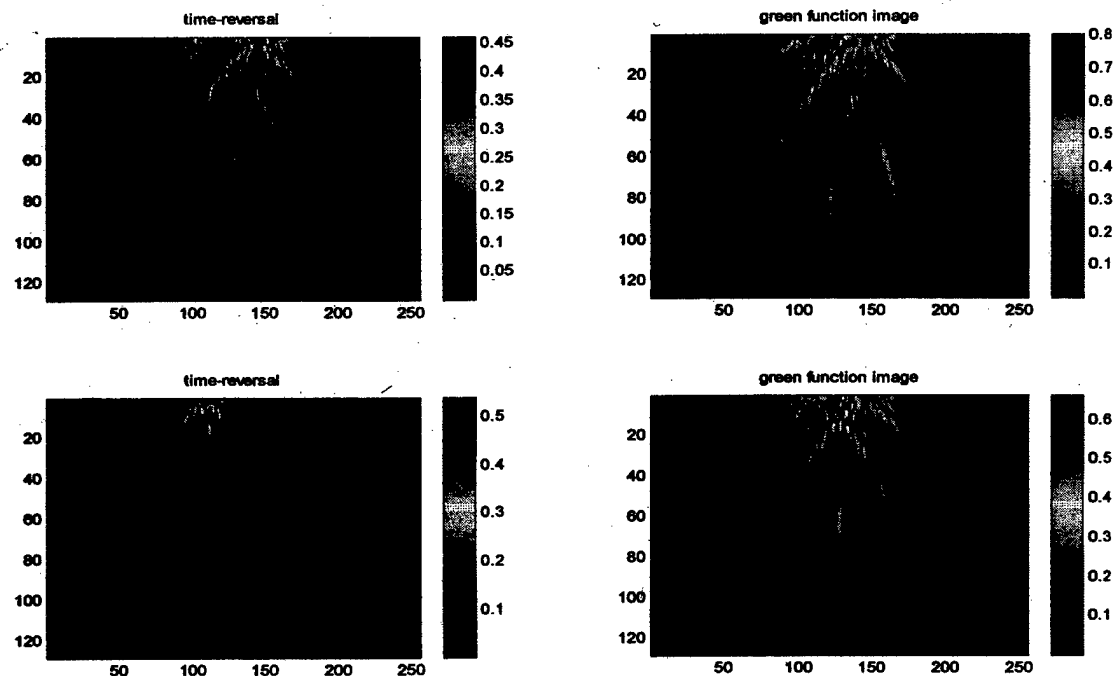


Figure 10: (Left) Images generated by the two eigenvectors shown in Fig. 9 and (right) images generated by the complex conjugate Green function vectors shown in Fig. 9. The "X" on the images indicates the location of the targets.

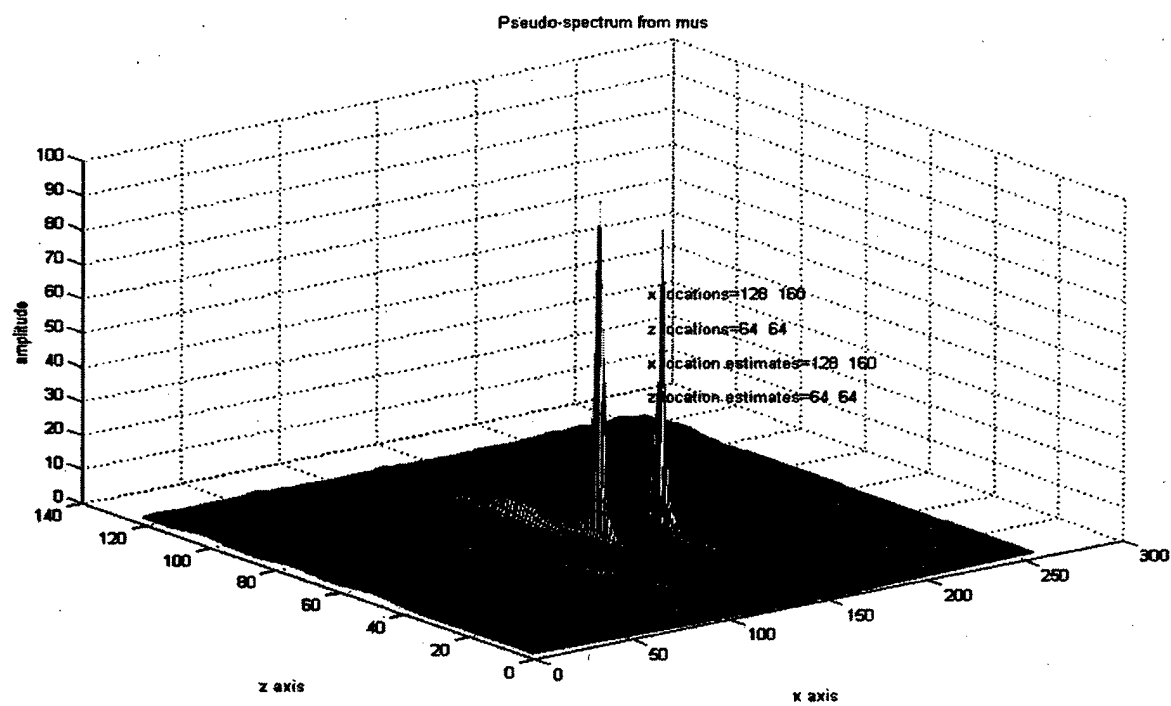


Figure 11: The pseudo-spectrum computed for the simulation depicted in Fig. 10. The peak values of the pseudo-spectrum are given as text in the figure and indicate that exact results were obtained for both the x and z location estimates.

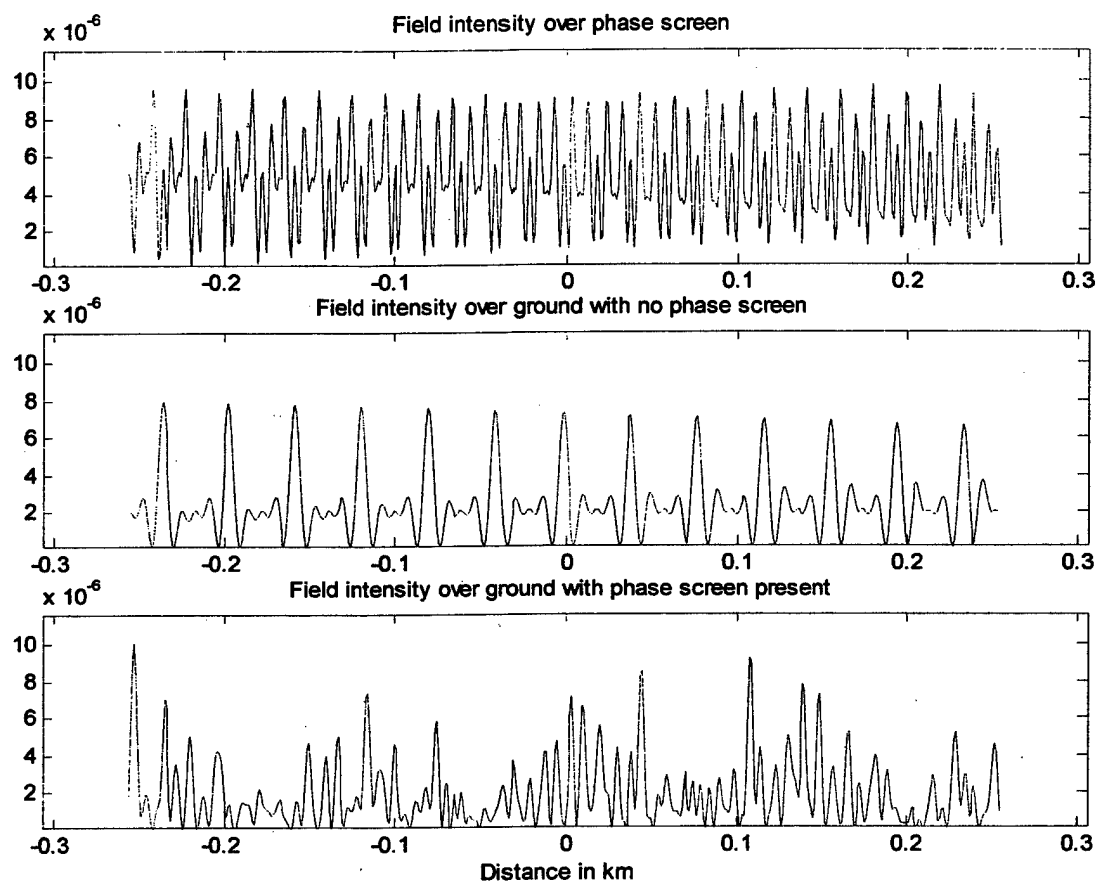


Figure 12: Plots of the field intensity over the phase screen (top), over the ground with no phase screen present (middle) and over the ground with a phase screen present (bottom).

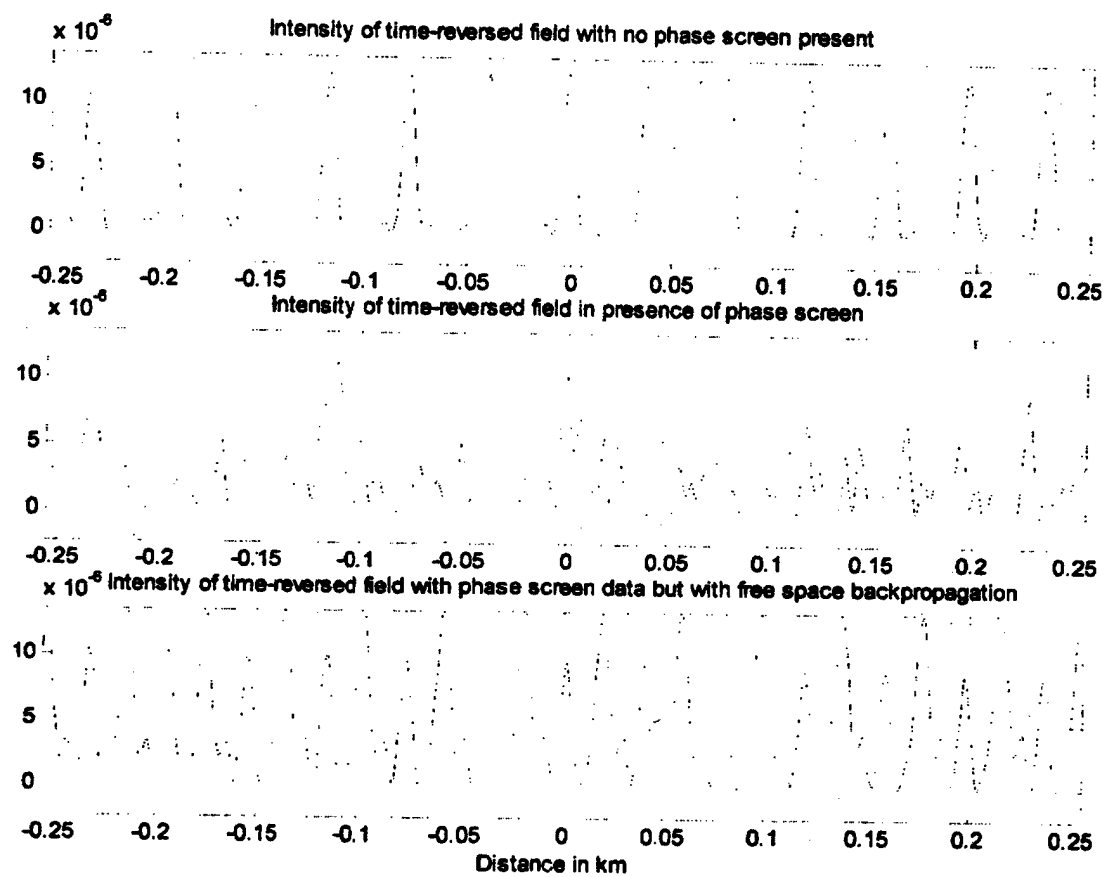


Figure 13: Plots of the intensity of the time-reversed field over the ground with no phase screen present, with phase screen present and with phase screen data but free space back propagation.

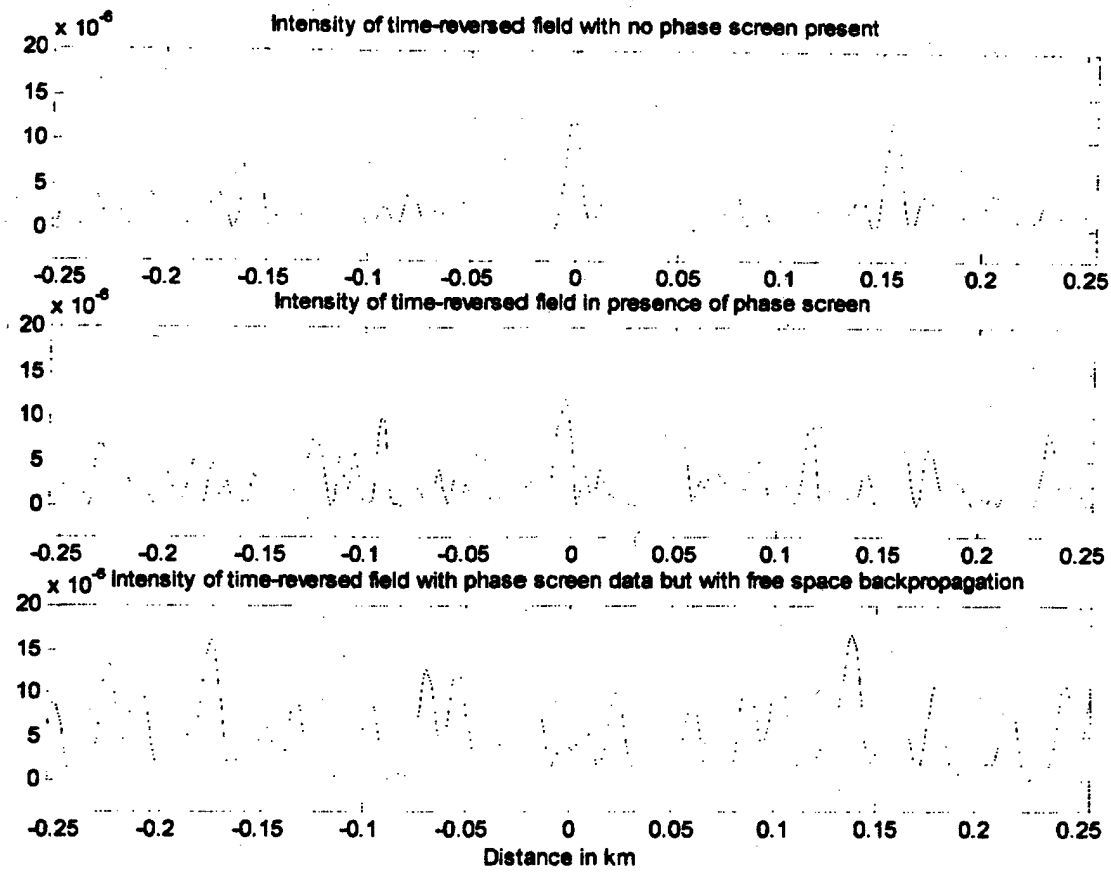


Figure 14: Same as for fig. 13 but with a different antenna geometry. Note the larger grating lobe period due to the smaller minimum separation between adjacent antenna elements.

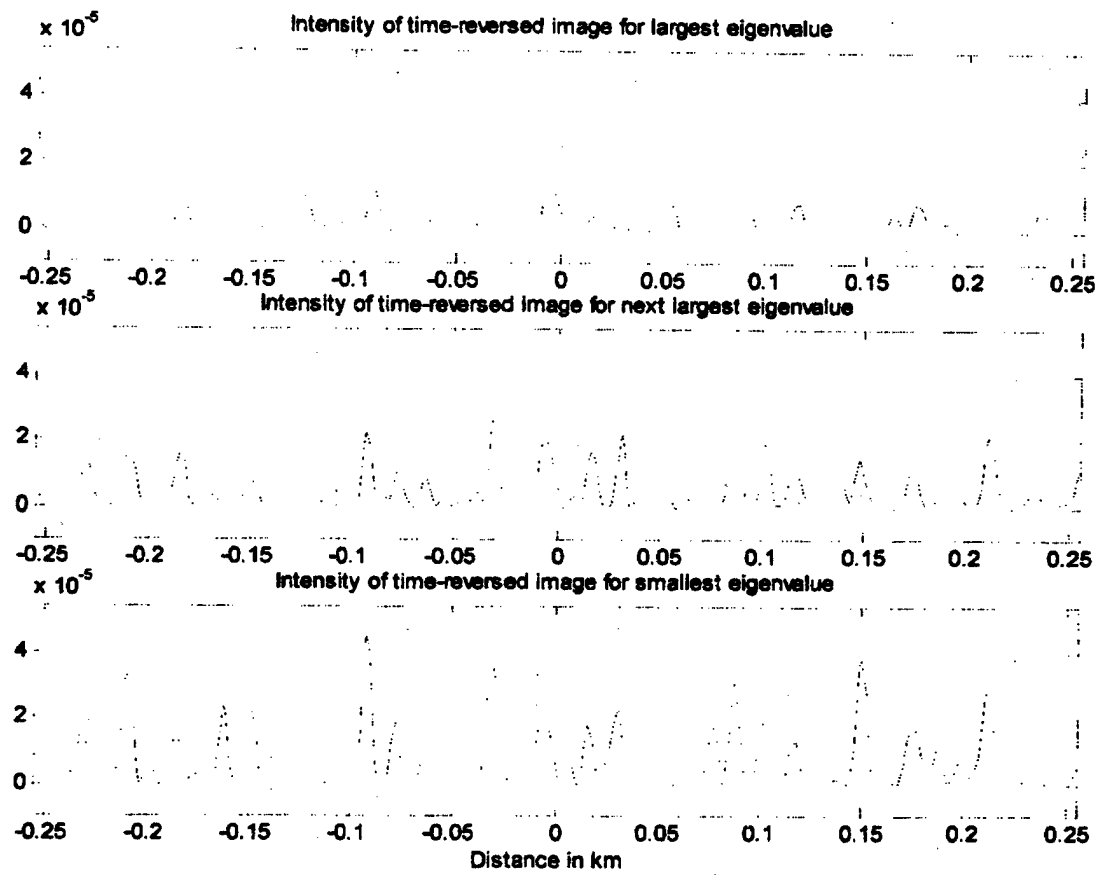
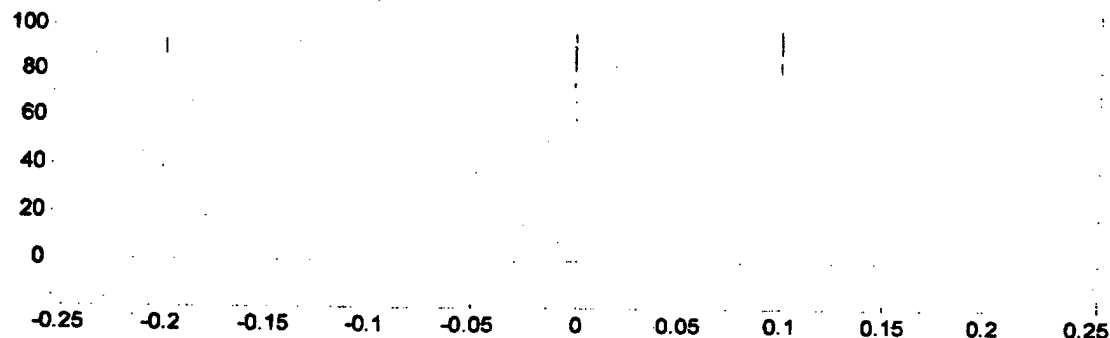


Figure 15: Plots of the intensity of the time-reversed field over the ground with a phase screen present for the cases of three targets located at $x_m = -200, 0$, and $+100$ meters.

Plot of the Pseudo-spectrum with no additive noise



Plot of the Pseudo-spectrum with additive noise

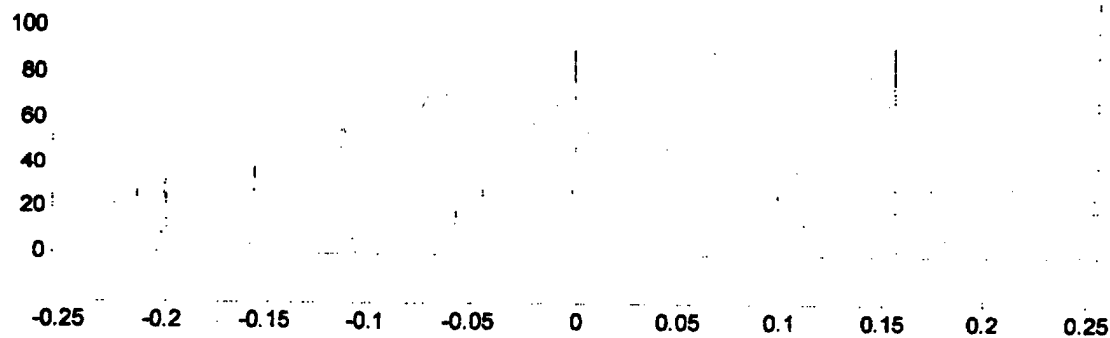
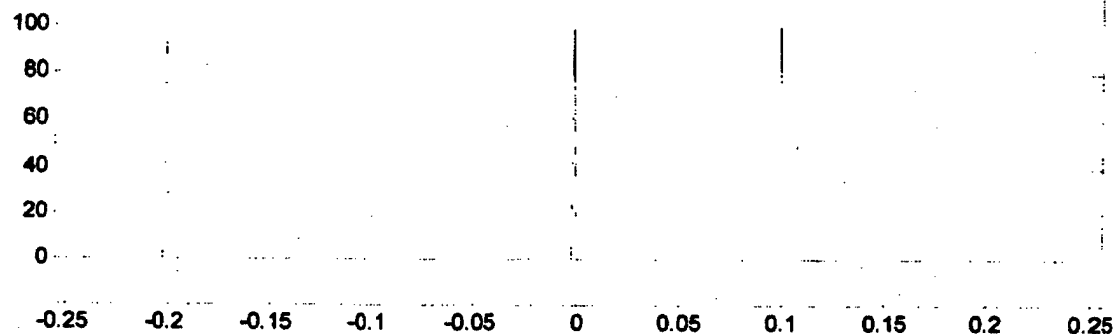


Figure 16: Plots of the pseudo-spectrum corresponding to the same conditions and set of parameters used for the conventional time-reversal images presented in 15 but with no phase screen present. The top plot is the pseudo-spectrum without additive noise while the bottom had additive noise with a noise amplitude $A_1 = 0.1$.

Plot of the Pseudo-spectrum with no additive noise



Plot of the Pseudo-spectrum with additive noise

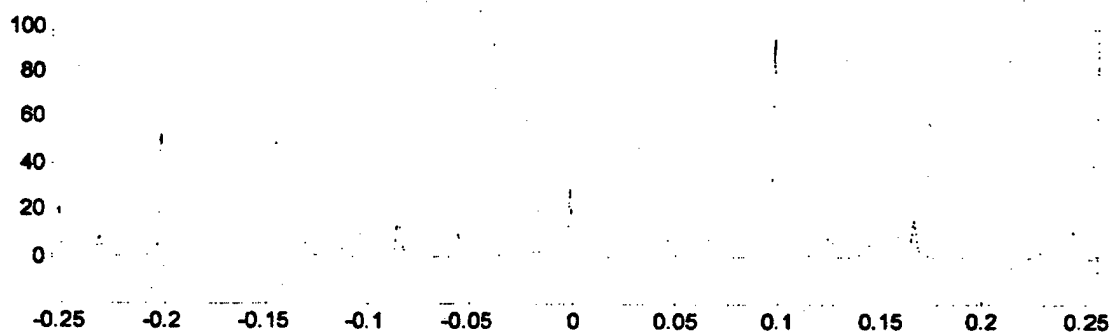
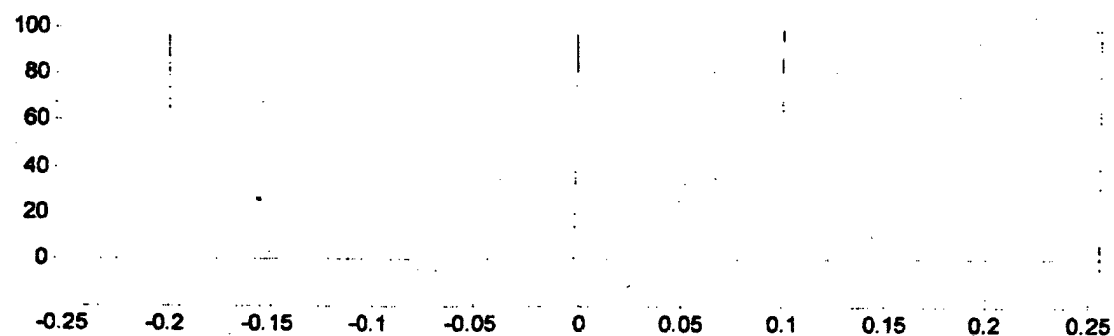


Figure 17: Same as in fig. 16 but with a phase screen present.

Plot of the Pseudo-spectrum-using phase screen steering vector



Plot of the Pseudo-spectrum-using free space steering vector

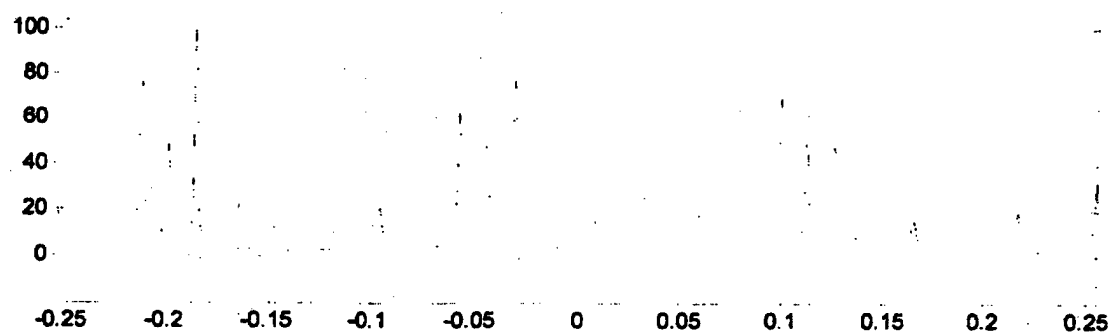
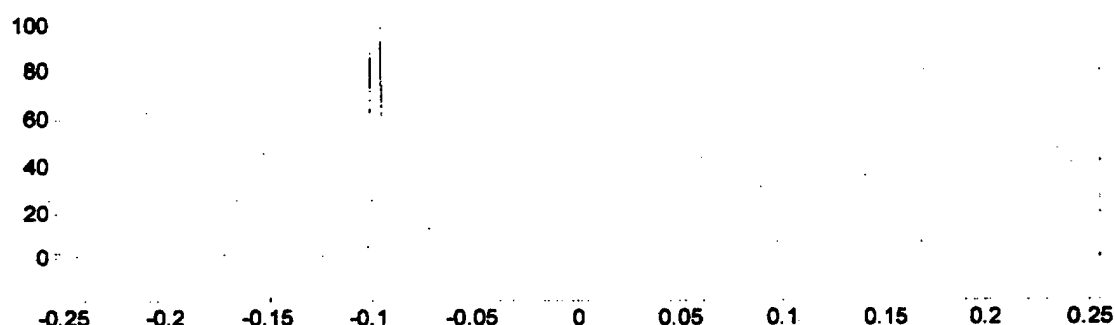


Figure 18: Plots of the noise free pseudo-spectrum corresponding to the same parameters used in fig. 17. The top plot is the pseudo-spectrum computed with the correct steering vector while the bottom plot uses the free space steering vector.

Plot of the Pseudo-spectrum with no additive noise



Plot of the Pseudo-spectrum with additive noise

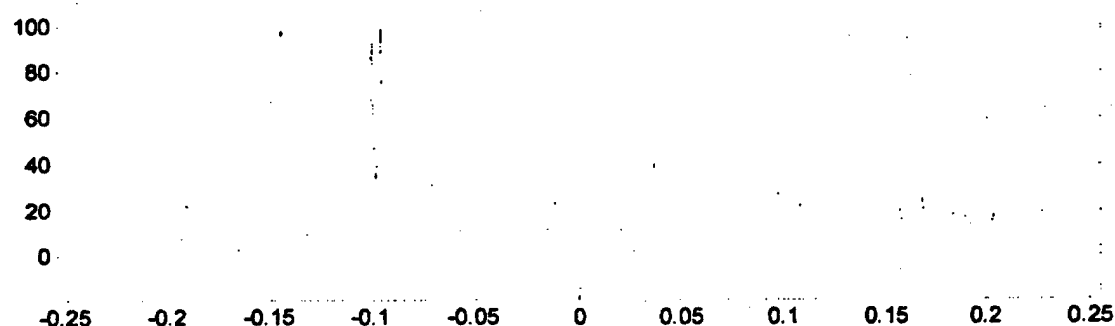


Figure 19: Plots of the pseudo-spectrum resulting for two real targets and eight clutter targets. The top plot is the pseudo-spectrum for the no noise case while the bottom plot is the pseudo-spectrum for an additive noise with amplitude $A_1 = 0.1$.